Open-Circuit Fault Research on Asymmetric Delta-Polygon 18-Pulse Autotransformer Rectifier Unit for More Electric Aircraft

Chao Yang, Fanghua Zhang, *Member, IEEE*, Long Cheng, and Zhaorong Zhang

***Abstract*—In aviation aircraft, autotransformer rectifier units (ATRUs) have been widely used as front-end rectifiers. The comprehensive analysis of its operating characteristics under the fault is beneficial to assessing the hazards of the faults and developing a fault diagnosis scheme. This article investigates two types of open-circuit (OC) faults in delta-polygon 18-pulse ATRU, namely, diode OC fault and input OC fault. First, the effects of the diode OC fault on five aspects are quantitatively analyzed: diode conduction angle, output voltage ripple, winding current, input current harmonics, and diode and transformer winding losses. Next, the operating characteristics of ATRU are investigated under input OC fault, and the quantitative effects of the five aspects above are also calculated. Then, based on the affected intervals of dc output voltage, a fault diagnosis idea dealing with two types of OC faults is discussed. Meanwhile, the predictive maintenance objects after the fault location are also summarized. Finally, the simulation and experimental results validate the theoretical analysis and discussion. This work is very significant for guiding the fault detection, fault location, and predictive maintenance of ATRUs.**

***Index Terms*—Autotransformer rectifier units (ATRUs), diode open-circuit (OC) fault, fault diagnosis, input OC fault, predictive maintenance, quantitative analysis.**

I. Introduction

With the development of more electric aircraft and all-electric aircraft, more and more schemes using hydraulic or pneumatic energy to realize the specific functions (e.g., wing-ice protection, environment control, flight control) have been replaced by electrical schemes [1]. The significant increase in demand for dc power energy necessitates a front-end rectifier with large capacity, high efficiency, small size, less weight, and low cost. In this context, multipulse autotransformer rectifier units (ATRUs), which effectively eliminate the harmonics in input current and reduce the output voltage ripple when compared to a three-phase diode bridge rectifier, have attracted the extensive attention of many researchers and engineers [2], [3].

According to the number of rectification pulses, ATRUs can be categorized into 12- [4], [5], 18- [6]–[8], 24-pulse [9], or even more pulses [10], [11], and the theoretical total harmonic distortion (THD) values of their input current are 15.2%, 10.1%, 7.6%, or even lower, respectively. Apparently, as the number of pulses increases, the THD value of the input current decreases gradually. While the configuration of the phase-shifting transformer becomes more complicated, which increases the manufacturing difficulties. Some aviation standards, such as ISO-1540 [12] and DO160-F [13], require that the THD of the input line current for three-phase equipment be strictly maintained within 10%, as high harmonic emission levels may interfere with the normal operation of other loads. Therefore, considering the tradeoff between the current THD and transformer configuration complexity, the 18-pulse ATRUs are the most appropriate choice for aviation aircraft. In addition, in [14] and [15], the research on the different 18-pulse ATRUs has confirmed that the asymmetric delta-polygon (DP) type has the lowest kilovolt ampere (kVA) rating, which means that the volume and weight of the phase-shifting transformer can be greatly reduced. Hence, the asymmetric DP 18-pulse ATRU is widely employed in aviation aircraft with stringent weight, volume, and power quality requirements.

Apart from the normal operation, the characteristics of the 18-pulse ATRU under the fault conditions should also be considered due to the comprehensive performance evaluation. In general, the overcurrent phenomenon caused by a short-circuit fault can be detected immediately and eliminated by the fuse. However, the open-circuit (OC) fault does not cause the ATRUs to shut down immediately but continues to operate with poor performance, which may cause some devices to suffer from increased stress, resulting in a secondary fault [16]. Diode and input OC faults are two types of typical OC faults in ATRUs. For diode OC fault, in [17], a diode OC fault diagnosis method based on the local and global minimum values of output voltage for the 12-pulse parallel and series TRU was presented. However, to avoid the complex calculation of the output voltage in [17], a diode OC fault diagnosis method using Hausdorff distance algorithm to extract the fault feature of the output voltage sag for an 18-pulse ATRU was proposed [18]. Recently, considering the

Manuscript received 21 January 2022; revised 5 May 2022; accepted 30 June 2022. Date of publication 11 July 2022; date of current version 6 September 2022. This work was supported by the National Natural Science Foundation of China under Grant 51777094. Recommended for publication by Associate Editor A. Barrado. *(Corresponding author: Fanghua Zhang.)*

Chao Yang, Fanghua Zhang, and Zhaorong Zhang are with the College of Automation Engineering, Nanjing University of Aeronautics and Astronautics, Nanjing 210016, China (e-mail: yangc@nuaa.edu.cn; zhangfh@nuaa.edu.cn; zhaorong@nuaa.edu.cn).

Long Cheng is with the Department of Electrical Engineering, Anhui Agricultural University, Hefei 230036, China (e-mail: cl@ahau.edu.cn).

Color versions of one or more figures in this article are available at https://doi.org/10.1109/TPEL.2022.3189502.

Digital Object Identifier 10.1109/TPEL.2022.3189502

use of the single passive harmonic reduction technology in the multipulse rectifiers, the output voltage for parallel-connected 24-pulse rectifier under diode OC fault in the main circuit and dc-side passive harmonic reduction circuit was analyzed in [19], and then feature parameters reflecting diode fault information were determined. In [20], the output voltage of the 36-pulse ATRU with the dual passive harmonic reduction circuit has also been analyzed for the fault features. In addition, some intelligence algorithms are used to diagnose diode OC faults in different ATRUs. In [21], a diode OC fault diagnosis method integrating artificial neural networks, wavelet packet decomposition, and principal component analysis for a 24-pulse ATRU was proposed, in which the wavelet packet decomposition algorithm is used to extract the fault features of the output voltage waveform. In [22], a diode OC fault diagnosis method using radial basis function network groups to identify the output voltage fault features for 12-pulse ATRU was proposed. The aforementioned research on diode OC fault has a common characteristic, that is, they all pay more attention to the output voltage to develop a fault diagnosis scheme, which is obviously not inadequate in terms of the performance evaluation of ATRUs under the fault condition. For input OC fault, in [23] and [24], the input OC faults of 12-pulse ATRUs with an active inter-phase reactor based on the delta- and zigzag-connected autotransformer are investigated, respectively. However, the influence of the input OC fault on the performance of asymmetric DP 18-pulse ATRU is still unclear, and thus a detailed analysis is necessary.

Through the above review, previous work cannot help researchers and engineers fully comprehend the effects and harm of OC faults since the original purpose of their work is only to determine fault features to develop fault diagnosis methods. Meanwhile, the single fault diagnosis cannot guide the predictive maintenance of the equipment after fault diagnosis. In fact, many interesting performance indicators of ATRUs under fault conditions should be comprehensively and quantitatively evaluated. Unfortunately, these contents are still rare in existing research.

In this article, the asymmetric DP 18-pulse ATRU is taken as the research object. The comprehensive influences and the diagnosis idea of the typical two types of OC faults (diode and input OC faults) are analyzed and discussed. This work not only clarifies the operating characteristics of ATRU under OC fault but also is beneficial for developing a fault diagnosis scheme and digging the predictive maintenance objects. Moreover, the analysis framework and approach of this paper can be easily generalized to be extended to other multipulse rectifiers. The rest of this article is organized as follows: Section II describes the normal operation mode of ATRU. In Section III, the effects of the different diode OC faults on five aspects: diode conduction angle, output voltage ripple, winding current, input current harmonics, and losses of diode and winding are analyzed quantitatively. In Section IV, the changes in the operating characteristics of ATRU under input OC fault are explored, and its influences on the above five aspects are also analyzed. In Section V, combining the analysis results in Sections III and IV, a fault diagnosis idea dealing with two types of OC faults based on the affected intervals of dc output voltage is discussed. In Section VI, the simulation and experiment are implemented to verify the correctness of the theoretical analysis and discussion. In the end, the conclusion is presented in Section VII.

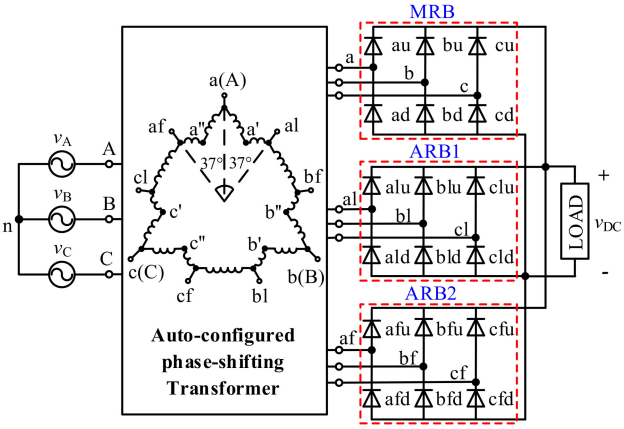

Fig. 1. Topology of the asymmetric DP 18-pulse ATRU.

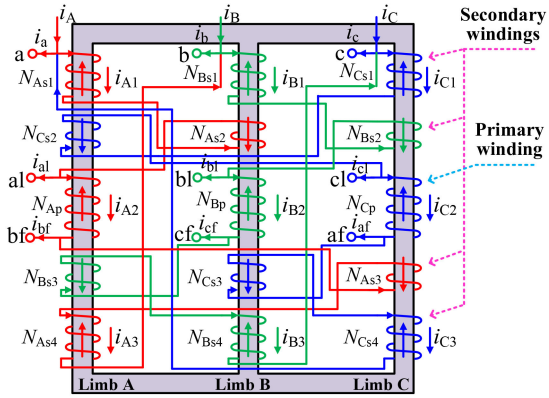

Fig. 2. Winding configuration of the phase-shifting transformer.

II. Normal Operation Analysis of DP 18-Pulse ATRU

This section analyzes the normal operation mode of DP 18-pulse ATRU, which can provide a theoretical foundation and reference for the later analysis of the fault operation and the discussion of the fault diagnosis idea.

Fig. 1 shows the topology of the asymmetric DP 18-pulse ATRU that is composed of a phase-shifting transformer, a main rectifier bridge (MRB), and two auxiliary rectifier bridges (ARB). Phase-shifting transformers are used to modify the magnitude and phase of the three-phase input voltage. The three rectifier bridges that the output terminals are directly paralleled convert ac to dc to power the load. Fig. 2 shows the placement of the windings of the phase-shifting transformer on a three-limb core. As can be seen, each limb has five windings, for instance, the primary winding N_{Cp} and the four secondary windings N_{Cs1}, N_{Bs2}, N_{As3}, and N_{Cs4} on limb C. Fig. 3 shows the phasor diagram of the phase-shifting transformer. Assuming that three-phase input voltages are as follows:

$$\begin{cases} v_{\mathrm{A(a)}} = \sqrt{2}V\sin(\omega t + \pi/2) \\ v_{\mathrm{B(b)}} = \sqrt{2}V\sin(\omega t - \pi/6) \\ v_{\mathrm{C(c)}} = \sqrt{2}V\sin(\omega t + 7\pi/6) \end{cases} \tag{1}$$

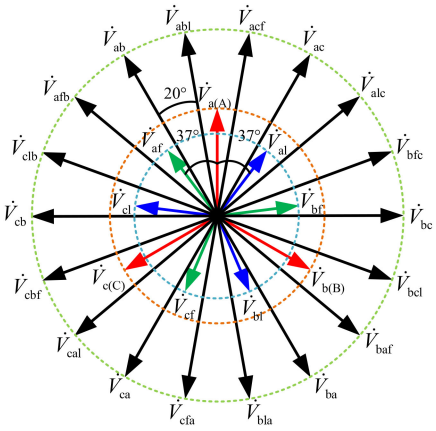

Fig. 3. Phasor diagram of the phase-shifting transformer.

where V is the root mean square (RMS) value of input phase voltage. According to the phasor diagram in Fig. 3, the other two sets of three-phase output voltages of the phase-shifting transformer can be written as

$$\begin{cases} v_{\rm al} = \sqrt{2}KV\sin(\omega t + \pi/2 - \theta_{\rm p}) \\ v_{\rm bl} = \sqrt{2}KV\sin(\omega t - \pi/6 - \theta_{\rm p}) \\ v_{\rm cl} = \sqrt{2}KV\sin(\omega t + 7\pi/6 - \theta_{\rm p}) \\ v_{\rm af} = \sqrt{2}KV\sin(\omega t + \pi/2 + \theta_{\rm p}) \\ v_{\rm bf} = \sqrt{2}KV\sin(\omega t - \pi/6 + \theta_{\rm p}) \\ v_{\rm cf} = \sqrt{2}KV\sin(\omega t + 7\pi/6 + \theta_{\rm p}) \end{cases} \tag{2}$$

where $K = 0.767$ and $\theta_{\rm p} = 37\pi/180$ [15]. Ignoring transformer leakage inductance and diode conduction voltage drop, the instantaneous value of dc output voltage under the continuous conduction mode can be expressed as

$$\begin{aligned} v_{\rm DC} = {} & S_{\rm a}v_{\rm a} + S_{\rm al}v_{\rm al} + S_{\rm af}v_{\rm af} + S_{\rm b}v_{\rm b} + S_{\rm bl}v_{\rm bl} \\ & + S_{\rm bf}v_{\rm bf} + S_{\rm c}v_{\rm c} + S_{\rm cl}v_{\rm cl} + S_{\rm cf}v_{\rm cf} \end{aligned} \tag{3}$$

where $S_{\rm a}$, $S_{\rm al}$, $S_{\rm af}$, $S_{\rm b}$, $S_{\rm bl}$, $S_{\rm bf}$, $S_{\rm c}$, $S_{\rm cl}$, and $S_{\rm cf}$ are switching functions of 9 bridge arms in Fig. 1. According to Fig. 3 or the voltage relations (1) and (2), the switching function of each bridge arm in the interval $\omega t \in [0, 2\pi)$ can be determined as follows:

$$S_{\rm a} = \begin{cases} 1 & \omega t \in [0, 2\pi/9) \cup [16\pi/9, 2\pi) \\ -1 & \omega t \in [7\pi/9, 11\pi/9) \\ 0 & \text{other} \end{cases}$$

$$S_{\rm al} = \begin{cases} 1 & \omega t \in [2\pi/9, \pi/3) \\ -1 & \omega t \in [11\pi/9, 4\pi/3) \\ 0 & \text{other} \end{cases}$$

$$\begin{aligned} & S_{\rm b} = S_{\rm a}\angle -2\pi/3, \quad S_{\rm af} = S_{\rm al}\angle 5\pi/9 \\ & S_{\rm c} = S_{\rm al}\angle 2\pi/3, \quad S_{\rm bf} = S_{\rm al}\angle -\pi/9 \\ & S_{\rm bl} = S_{\rm al}\angle -2\pi/3, \quad S_{\rm cf} = S_{\rm al}\angle -7\pi/9 \\ & S_{\rm cl} = S_{\rm al}\angle 2\pi/3 \end{aligned} \tag{4}$$

where $S_{\rm x} = 1$ and -1 (x = a, al, af, b, bl, bf, c, cl, cf) represent the upper and lower diodes of bridge arm x are conducting, respectively, and $S_{\rm x} = 0$ means that two diodes on bridge arm x are OFF. Substituting (1), (2), and (4) into (3), the dc output voltage waveform (blue line) is plotted in Fig. 4. It can be observed that the output voltage is a pulsating dc with 18 subwaveforms and the first subwaveform is the wave crest of the line-to-line voltage $v_{\rm acf}$.

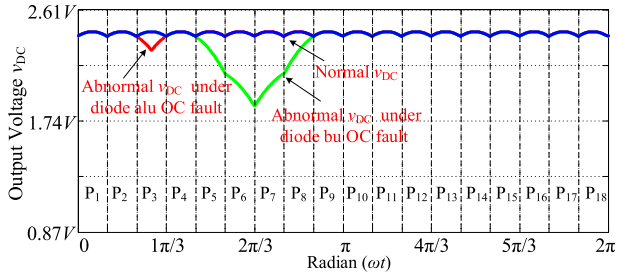

Fig. 4. DC output voltage waveforms under the normal operation and diode OC faults.

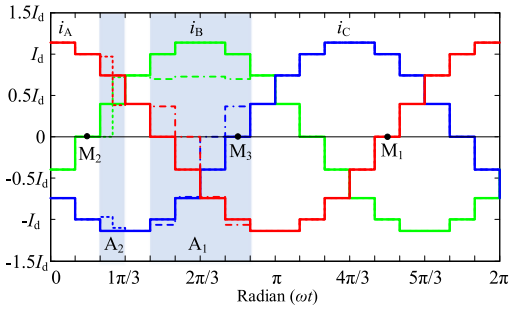

Fig. 5. Waveforms of three-phase input current under normal operation and diode OC faults.

Furthermore, noted that the windings $N_{X\rm p}$ (X = A, B, C) are equal in Fig. 2 and $N_{X\rm s1} = N_{X\rm s4}$, $N_{X\rm s2} = N_{X\rm s3}$. According to the ampere-turn balance theory and Kirchhoff's current law, the following relations can be obtained:

$$\begin{cases} N_{\rm As1}i_{\rm A1} + N_{\rm Ap}i_{\rm A2} + N_{\rm As1}i_{\rm A3} = N_{\rm As2}i_{\rm C1} + N_{\rm As2}i_{\rm B3} \\ N_{\rm As1}i_{\rm B1} + N_{\rm Ap}i_{\rm B2} + N_{\rm As1}i_{\rm B3} = N_{\rm As2}i_{\rm A1} + N_{\rm As2}i_{\rm C3} \\ N_{\rm As1}i_{\rm C1} + N_{\rm Ap}i_{\rm C2} + N_{\rm As1}i_{\rm C3} = N_{\rm As2}i_{\rm B1} + N_{\rm As2}i_{\rm A3} \end{cases} \tag{5}$$

$$\begin{cases} i_{\rm A} = i_{\rm a} + i_{\rm A1} - i_{\rm C3} \\ i_{\rm B} = i_{\rm b} + i_{\rm B1} - i_{\rm A3} \\ i_{\rm C} = i_{\rm c} + i_{\rm C1} - i_{\rm B3} \end{cases} \begin{cases} i_{\rm al} = i_{\rm A1} - i_{\rm A2} \\ i_{\rm bl} = i_{\rm B1} - i_{\rm B2} \\ i_{\rm cl} = i_{\rm C1} - i_{\rm C2} \end{cases} \begin{cases} i_{\rm af} = i_{\rm C2} - i_{\rm C3} \\ i_{\rm bf} = i_{\rm A2} - i_{\rm A3} \\ i_{\rm cf} = i_{\rm B2} - i_{\rm B3} \end{cases} \tag{6}$$

where $N_{\rm As1}$, $N_{\rm As2}$, and $N_{\rm Ap}$ can be derived from the geometric relation in Fig. 3 [15]. They are 0.4472, 0.2381, and 0.6015, respectively, when the turns of virtual winding corresponding to input phase A voltage are marked 1. Assuming that the load current is constant $I_{\rm d}$, in combination with (4)–(6), three-phase input current waveforms (solid line) can be plotted in Fig. 5. Obviously, the input current is an approximate sine wave with 18 steps in one period.

III. Diode OC Fault Analysis of DP 18-Pulse ATRU

This section analyzes the influences of the different diode OC faults on the five aspects. According to (4), each diode in MRB

conducts 80° while each diode in ARB1 and ARB2 conducts 20°. Therefore, the diode OC faults can be divided into two types: diode OC fault in MRB and diode OC fault in ARB, and they should be analyzed separately. Here the diode bu OC fault in MRB and diode alu OC fault in ARB are taken as examples to reveal the mechanism of their influences on the performance of the rectifier.

A. Diode Conduction Angle Analysis Under Diode OC Fault

When the diode bu OC fault in MRB occurs, in its working period $\omega t\in[4\pi/9, 8\pi/9)$, the wave crests of the four line-to-line voltages associated with diode bu cannot be delivered to the dc side due to the absence of a path to the output. From the perspective of the time axis, in the interval $\omega t\in[4\pi/9, 8\pi/9)$, the upper diodes closest to the working interval of the faulty diode bu will operate instead of it. This causes the second maximum instantaneous voltage to be output. Consequently, the switching functions of three bridge arms (b, bf, and bl) related to diode bu OC fault are changed as follows:

$$S_{\mathrm{b-buF}} = \begin{cases} -1 \ \omega t \in [13\pi/9, 17\pi/9) \\ 0 \quad \text{other} \end{cases} \tag{7}$$

$$S_{\mathrm{bf-buF}} = \begin{cases} 1 \ \omega t \in [\pi/3, 2\pi/3) \\ -1 \ \omega t \in [4\pi/3, 13\pi/9) \\ 0 \quad \text{other} \end{cases} \tag{8}$$

$$S_{\mathrm{bl-buF}} = \begin{cases} 1 \ \omega t \in [2\pi/3, \pi) \\ -1 \ \omega t \in [17\pi/9, 2\pi) \\ 0 \quad \text{other} \end{cases}. \tag{9}$$

From (7)–(9), the conduction angle 80° of diode bu is shared equally by diodes bfu and blu, whose conduction angles are changed from 20° to 60°.

Similarly, when the diode alu OC fault in ARB occurs, the diodes au and bfu that are closest to its working interval $\omega t\in[2\pi/9, \pi/3)$ will replace it. Also, they share the conduction angle 20° of the faulty diode alu equally. Thus, the conduction angles of diodes au and bfu become 90° and 30°, respectively. As a result, the switching functions of three bridge arms (al, a, and bf) associated with diode alu OC fault are changed as follows:

$$S_{\mathrm{al-aluF}} = \begin{cases} -1 \ \omega t \in [11\pi/9, 4\pi/3) \\ 0 \quad \text{other} \end{cases} \tag{10}$$

$$S_{\mathrm{a-aluF}} = \begin{cases} 1 \ \omega t \in [0{,}5\pi/18) \cup [16\pi/9, 2\pi) \\ -1 \ \omega t \in [7\pi/9, 11\pi/9) \\ 0 \quad \text{other} \end{cases} \tag{11}$$

$$S_{\mathrm{bf-aluF}} = \begin{cases} 1 \ \omega t \in [5\pi/18, 4\pi/9) \\ -1 \ \omega t \in [4\pi/3, 13\pi/9) \\ 0 \quad \text{other} \end{cases}. \tag{12}$$

B. Output Voltage Ripple Analysis Under Diode OC Fault

From Fig. 4, it is easy to know that the output voltage ripple under the normal operation is the difference between maximum and minimum at 20° wave crest of the line-to-line voltage, and it can be expressed as

$$V_{\mathrm{R-NOR}} = \sqrt{2}V_{\mathrm{bc}}(1 - \cos 10^\circ) \approx 0.0372\,V \tag{13}$$

where $V_{\mathrm{bc}} = 1.732\,V$ [15]. According to (3), (4), (7)–(9), and (10)–(12), the dc output voltage waveforms under diodes bu and alu OC faults are plotted in Fig. 4, respectively. It can be seen from Fig. 4 that in the interval $\omega t\in[4\pi/9, 8\pi/9)$, the wave crests of the four voltages (v_{bc}, v_{bcl}, v_{baf}, v_{ba}) are not delivered to the dc side under diode bu OC fault. According to Fig. 3, the line-to-line voltage with the second maximum instantaneous value is v_{bfc} in the interval $\omega t\in[4\pi/9, 5\pi/9)$, hence, the part waveform of the voltage v_{bfc} is output in the interval $\omega t\in[4\pi/9, 5\pi/9)$. Likewise, in the interval $\omega t\in[5\pi/9, 2\pi/3)$, the line-to-line voltage with the second maximum instantaneous value is v_{bfcl}, thereby the part waveform of the voltage v_{bfcl} is output in the interval $\omega t\in[5\pi/9, 2\pi/3)$. Meanwhile, in the intervals $\omega t\in[2\pi/3, 7\pi/9)$ and $[7\pi/9, 8\pi/9)$, the part waveforms of the voltages v_{blaf} and v_{bla} are output, respectively. Consequently, a sag with a width of 80° appears in the interval $\omega t\in[4\pi/9, 8\pi/9)$ of the dc output voltage, as shown in Fig. 4. The minimum voltage that this sag can reach is calculated as

$$V_{\mathrm{min-buF}} = \sqrt{2}V_{\mathrm{bfcl}}\cos(30^\circ) \approx 1.8649\,V \tag{14}$$

where $V_{\mathrm{bfcl}} = 0.8791V_{\mathrm{bc}}$ can be derived from Fig. 3. Thus, the output voltage ripple under diode bu OC fault can be calculated as

$$V_{\mathrm{R-buF}} = \sqrt{2}V_{\mathrm{bc}} - \sqrt{2}V_{\mathrm{bfcl}}\cos(30^\circ) \approx 0.5846\,V. \tag{15}$$

Similarly, when the diode alu OC fault occurs, the voltage v_{ac} is output by the diodes au and cd in the left-half interval $\omega t\in[2\pi/9, 5\pi/18)$ of the working interval $\omega t\in[2\pi/9, \pi/3)$ of the faulty diode alu, and the voltage v_{bfc} is output by the diodes bfu and cd in the right-half interval $\omega t\in[5\pi/18, \pi/3)$. Hence, a 20° sag appears in the interval $\omega t\in[2\pi/9, \pi/3)$ of the dc output voltage. The minimum value of this sag is calculated as

$$V_{\mathrm{min-aluF}} = \sqrt{2}V_{\mathrm{ac}}\cos(20^\circ) \approx 2.3018\,V. \tag{16}$$

Consequently, the output voltage ripple under diode alu OC fault can be calculated as

$$V_{\mathrm{R-aluF}} = \sqrt{2}V_{\mathrm{ac}} - \sqrt{2}V_{\mathrm{ac}}\cos(20^\circ) \approx 0.1477\,V. \tag{17}$$

From (13), (15), and (17), it can be found that the output voltage ripple caused by diode OC fault in MRB and ARB is about 15.7 times and 4 times that of the normal operation, respectively, which seriously exceeds the dc voltage ripple requirement of the relevant standards.

C. Winding Current Analysis Under Diode OC Fault

Under diode OC fault, the winding current of the transformer will diverge from the normal operation curve. It can be known from Section III-B that at the positions of 80° and 20° sags caused by diodes bu and alu OC faults, the load current also declines with the voltage drop and is less than the constant current I_{d}. To simplify the calculation, the load current values at these positions are equivalently calculated as per the RMS value, which is presented in Appendix A.

Combining (4)–(12), the current curves of all winding under the normal operation (blue line), diode bu OC fault (green line), and diode alu OC fault (red line) are calculated and plotted

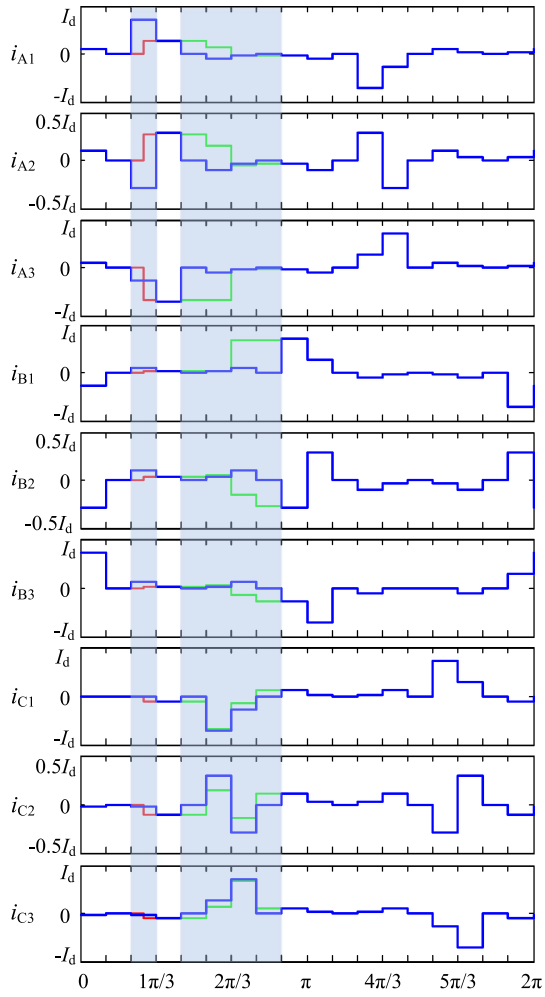

Fig. 6. Current waveforms of the windings under normal operation, diode bu OC fault, and diode alu OC fault.

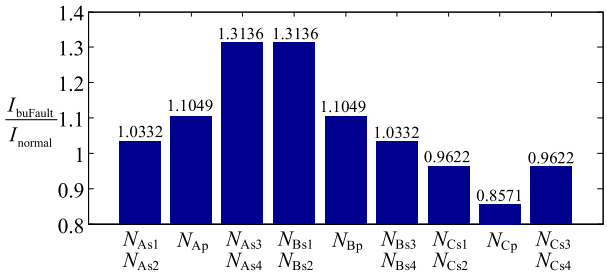

Fig. 7. Ratio of current RMS value for each winding after and before the diode bu fault.

in Fig. 6, respectively. For diode bu OC fault, it can be found from Fig. 6 that the affected interval of the winding current is $\omega t \in [4\pi/9, 8\pi/9)$, which is consistent with the position of 80° sag in the dc output voltage. Apparently, the current i_{A3} and i_{B1} are very different from the normal condition, followed by the current i_{A2} and i_{B2}. For diode alu OC fault, all winding current is disturbed in the interval $\omega t \in [2\pi/9, \pi/3)$, and the changes in currents i_{A1}, i_{A2}, and i_{A3} are relatively obvious.

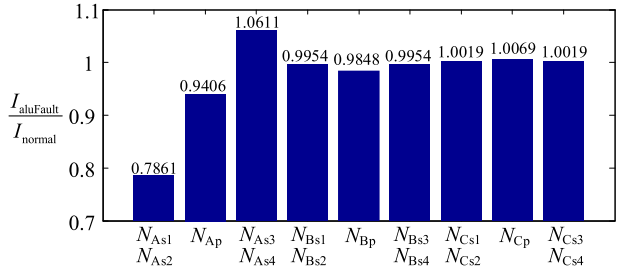

Fig. 8. Ratio of current RMS value for each winding after and before the diode alu fault.

Figs. 7 and 8 show the ratio of current RMS value for each winding after and before the diode bu and alu OC faults, respectively. From Fig. 7, the current of the windings N_{As3}, N_{As4}, N_{Bs1}, and N_{Bs2} increases significantly, which is 1.3 times the normal condition. Second, the current i_{A2} and i_{B2} for the windings N_{Ap} and N_{Bp} fewer increases and is 1.1 times the normal condition. For diode alu OC fault, only the current i_{A2} of the winding N_{As3} and N_{As4} increases slightly.

From the above analysis, the diode OC fault in MRB has a significant impact on the winding current, but the influence of the diode OC fault in ARB on the winding current is slight.

D. Input Line Current Analysis Under Diode OC Fault

Input line current is closely related to the winding current. According to (6) and the winding current in Section III-C, the theoretical waveforms of three-phase input current under diode bu OC fault (stippled line) and diode alu OC fault (dotted line) are also calculated and plotted in Fig. 5. From Fig. 5, the three-phase input current in the shaded areas A1 and A2 are disturbed by diodes bu and alu OC faults, respectively. When the diode bu is open, the wave crest of phase B input current is cut OFF, and another two-phase line current is also distorted in the interval $\omega t \in [4\pi/9, 8\pi/9)$ owing to $i_A + i_B + i_C = 0$. Due to the different impacts of the two intervals ($\omega t \in [2\pi/9, 5\pi/18)$ and $\omega t \in [5\pi/18, \pi/3)$) caused by diode alu OC fault in shaded area A2, the waveforms of the input line current for one cycle is equally divided into 36 parts. From Fig. 5, taking the midpoint M_1, M_2, and M_3 of positive and negative half-wave of phase A, B, and C current as the midpoint of one period for each input current, respectively, the current values of 36 intervals from left to right in one period of the three-phase input current under different conditions can be reorganized as b_i ($i = 1, 2, \ldots, 36$) and given in Appendix B. As a result, Fourier's series of three-phase input line current can be uniformly derived as

$$i_{A,B,C} = \frac{1}{36}\sum_{i=1}^{36}(b_i) + \sum_{n=1}^{\infty}\frac{2I_d}{n\pi}\sin\frac{n\pi}{36} \times \left\{ \begin{array}{l} \left[\sum_{i=1}^{18}(b_{37-i}+b_i)\cos\frac{(37-2i)n\pi}{36}\right]\cos(n\omega t) \\ +\left\{\left[\sum_{i=1}^{18}(b_{37-i}-b_i)\sin\frac{(37-2i)n\pi}{36}\right]\sin(n\omega t)\right\} \end{array} \right\}. \quad (18)$$

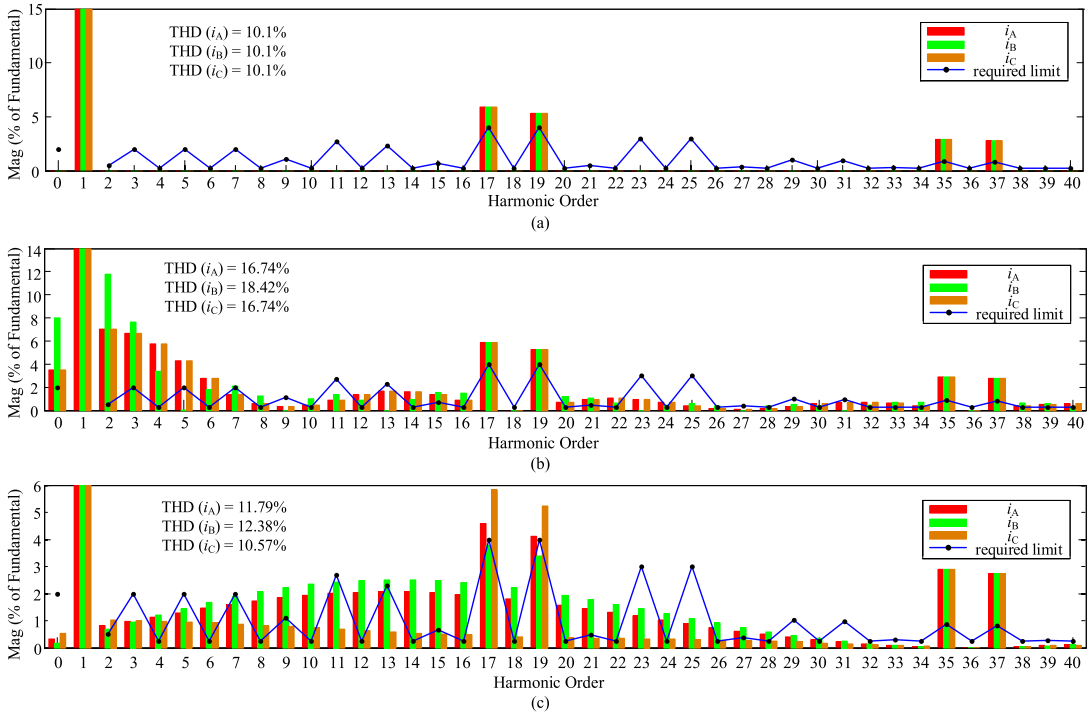

Fig. 9. Spectrum of the theoretical three-phase input current under the different cases. (a) Normal operation. (b) Diode bu OC fault. (c) Diode alu OC fault.

According to (18), the spectrum of three-phase input current under the normal operation, diode bu OC fault, and diode alu OC fault are plotted in Fig. 9(a)–(c), respectively.

For the normal operation, from Fig. 9(a), only $18k\pm1$ ($k = 1, 2\ldots$) order harmonics are involved in the three-phase current, which indicates that the multipulse rectification can indeed eliminate low-order harmonics to reduce input current THD.

For diode bu OC fault, it can be found from Fig. 9(b) that the THD values of three-phase input current are 16.74%, 18.42%, and 16.74%, respectively, which increases markedly in comparison to normal operation. Meanwhile, both the low-order odd harmonics with high amplitude and the low-order even harmonics with high amplitude are contained in the three-phase input current, which seriously pollutes the ac power grid. In a word, not only THD values of three-phase input current exceed the required limit (10%) in the standards ISO 1540 and DO-160F, but also the individual frequency components are beyond the required limit in standards. Moreover, due to asymmetrical positive and negative half-waves caused by diode bu OC fault, the dc component in three-phase input current increases greatly, especially in phase B current, the content is up to 8%.

As for diode alu OC fault, from Fig. 9(c), the THD values of the three-phase current are 11.79%, 12.38%, and 10.57%, respectively, which increases slightly compared with the normal operation. In addition, a substantial number of low-order harmonics, particularly even harmonics, are beyond the required limit. Meanwhile, due to the waveform cancellation of current i_A and i_B in the affected interval $\omega t\in[5\pi/18, \pi/3)$, the current i_C suffers less disturbance compared to i_A and i_B. Thus, only harmonics with low amplitude are generated.

E. Losses Analysis of Diode and Transformer Winding Under Diode OC Fault

1) Diode Losses:

① Under normal operation, the current average value (I_{MRBAV}, I_{ARBAV}) and RMS value (I_{MRBRMS}, I_{ARBRMS}) through each diode in MRB and ARB are derived in Appendix A. It can be known from the equivalent circuit of the diode that the conduction voltage drop across the diode consists of a constant threshold voltage V_{T} and voltage drop of a slope resistance R_{s}. Therefore, the losses of the single diode in MRB and ARB can be calculated as follows:

$$\begin{aligned} P_{\mathrm{SDMRB}} &= V_{\mathrm{T}} I_{\mathrm{MRBAV}} + I_{\mathrm{MRBRMS}}^2 R_{\mathrm{s}} = 2(V_{\mathrm{T}} I_{\mathrm{d}} + I_{\mathrm{d}}^2 R_{\mathrm{s}})/9 \\ P_{\mathrm{SDARB}} &= V_{\mathrm{T}} I_{\mathrm{ARBAV}} + I_{\mathrm{ARBRMS}}^2 R_{\mathrm{s}} = (V_{\mathrm{T}} I_{\mathrm{d}} + I_{\mathrm{d}}^2 R_{\mathrm{s}})/18. \end{aligned} \tag{19}$$

Then the total losses of 18 diodes can be obtained

$$P_{\mathrm{TD-NOR}} = 6 \times P_{\mathrm{SDMRB}} + 12 P_{\mathrm{SDARB}} = 2V_{\mathrm{T}} I_{\mathrm{d}} + 2I_{\mathrm{d}}^2 R_{\mathrm{s}}. \tag{20}$$

② Under diode bu OC fault, the current average value ($I_{\mathrm{bfuAV\text{-}buF}}$, $I_{\mathrm{bluAV\text{-}buF}}$, $I_{\mathrm{cdAV\text{-}buF}}$, $I_{\mathrm{adAV\text{-}buF}}$, $I_{\mathrm{cldAV\text{-}buF}}$, $I_{\mathrm{afdAV\text{-}buF}}$) and RMS value ($I_{\mathrm{bfuRMS\text{-}buF}}$, $I_{\mathrm{bluRMS\text{-}buF}}$, $I_{\mathrm{cdRMS\text{-}buF}}$, $I_{\mathrm{adRMS\text{-}buF}}$, $I_{\mathrm{cldRMS\text{-}buF}}$, $I_{\mathrm{afdRMS\text{-}buF}}$) of the affected six diodes bfu, blu, cd, ad, cld, and afd are also derived in Appendix A. The losses of these six diodes can be calculated as

$$\begin{aligned} P_{\mathrm{SDbfu-buF}} = P_{\mathrm{SDblu-buF}} &= V_{\mathrm{T}} I_{\mathrm{bfuAV-buF}} \\ &\quad + I_{\mathrm{bfuRMS-buF}}^2 R_{\mathrm{s}} \approx 0.1532 V_{\mathrm{T}} I_{\mathrm{d}} \\ &\quad + 0.1418 I_{\mathrm{d}}^2 R_{\mathrm{s}} \end{aligned}$$

$$P_{\mathrm{SDcd-buF}} = P_{\mathrm{SDad-buF}} = V_{\mathrm{T}} I_{\mathrm{cdAV-buF}} + I^2_{\mathrm{cdRMS-buF}} R_{\mathrm{s}} \approx 0.2186 V_{\mathrm{T}} I_{\mathrm{d}} + 0.2153 I^2_{\mathrm{d}} R_{\mathrm{s}}$$
$$P_{\mathrm{SDcld-buF}} = P_{\mathrm{SDafd-buF}} = V_{\mathrm{T}} I_{\mathrm{cldAV-buF}} + I^2_{\mathrm{cldRMS-buF}} R_{\mathrm{s}} \approx 0.0457 V_{\mathrm{T}} I_{\mathrm{d}} + 0.0376 I^2_{\mathrm{d}} R_{\mathrm{s}}. \quad (21)$$

Compared with (19), the losses of the diodes bfu and blu increase due to the increase in conduction angle induced by the diode bu OC fault, and the ratio of their corresponding losses after and before the fault can be calculated as

$$K_{\mathrm{SDbfu-buF}} = K_{\mathrm{SDblu-buF}} = P_{\mathrm{SDbfu-buF}} / P_{\mathrm{SDARB}}. \quad (22)$$

Meanwhile, the total losses of 17 diodes under diode bu fault can be calculated as

$$P_{\mathrm{TD-buF}} = 3P_{\mathrm{SDMRB}} + 8P_{\mathrm{SDARB}} + 2P_{\mathrm{SDbfu-buF}} + 2P_{\mathrm{SDcd-buF}} + 2P_{\mathrm{SDcld-buF}} \approx 1.9459 V_{\mathrm{T}} I_{\mathrm{d}} + 1.9004 I^2_{\mathrm{d}} R_{\mathrm{s}}. \quad (23)$$

Then the ratio of the total diode losses after and before diode bu OC fault is

$$K_{\mathrm{TD-buF}} = P_{\mathrm{TD-buF}} / P_{\mathrm{TD-NOR}}. \quad (24)$$

③ Under diode alu OC fault, the current average value ($I_{\mathrm{auAV\text{-}aluF}}$, $I_{\mathrm{cdAV\text{-}aluF}}$, $I_{\mathrm{bfuAV\text{-}aluF}}$) and RMS value ($I_{\mathrm{auRMS\text{-}aluF}}$, $I_{\mathrm{cdRMS\text{-}aluF}}$, $I_{\mathrm{bfuRMS\text{-}aluF}}$) of the affected three diodes au, cd, and bfu under diode alu fault are derived in Appendix A. The losses of these three diodes are calculated as

$$P_{\mathrm{SDau-aluF}} = V_{\mathrm{T}} I_{\mathrm{auAV-aluF}} + I^2_{\mathrm{auRMS-aluF}} R_{\mathrm{s}} \approx 0.2489 V_{\mathrm{T}} I_{\mathrm{d}} + 0.2481 I^2_{\mathrm{d}} R_{\mathrm{s}}$$
$$P_{\mathrm{SDcd-aluF}} = V_{\mathrm{T}} I_{\mathrm{cdAV-aluF}} + I^2_{\mathrm{cdRMS-aluF}} R_{\mathrm{s}} \approx 0.2203 V_{\mathrm{T}} I_{\mathrm{d}} + 0.2184 I^2_{\mathrm{d}} R_{\mathrm{s}}$$
$$P_{\mathrm{SDbfu-aluF}} = V_{\mathrm{T}} I_{\mathrm{bfuAV-aluF}} + I^2_{\mathrm{bfuRMS-aluF}} R_{\mathrm{s}} \approx 0.0824 V_{\mathrm{T}} I_{\mathrm{d}} + 0.0814 I^2_{\mathrm{d}} R_{\mathrm{s}}. \quad (25)$$

Compared with (19), the losses of the diodes au and bfu increase. The ratio of their losses after and before diode alu fault can be calculated as follows:

$$K_{\mathrm{SDau-aluF}} = P_{\mathrm{SDau-aluF}} / P_{\mathrm{SDMRB}}$$
$$K_{\mathrm{SDbfu-aluF}} = P_{\mathrm{SDbfu-aluF}} / P_{\mathrm{SDARB}}. \quad (26)$$

Consequently, the total losses for 17 diodes under diode alu fault are calculated as

$$P_{\mathrm{TD-aluF}} = 4P_{\mathrm{SDMRB}} + 10P_{\mathrm{SDARB}} + P_{\mathrm{SDau-aluF}} + P_{\mathrm{SDcd-aluF}} + P_{\mathrm{SDbfu-aluF}} \approx 1.9961 V_{\mathrm{T}} I_{\mathrm{d}} + 1.9923 I^2_{\mathrm{d}} R_{\mathrm{s}}. \quad (27)$$

TABLE I
RATIO OF DIODE LOSSES UNDER THE DIFFERENT DIODE OC FAULTS

Diode bu OC fault			Diode alu OC fault		
$K_{\mathrm{TD\text{-}buF}}$	$K_{\mathrm{SDbfu\text{-}buF}}$	$K_{\mathrm{SDblu\text{-}buF}}$	$K_{\mathrm{TD\text{-}aluF}}$	$K_{\mathrm{SDau\text{-}aluF}}$	$K_{\mathrm{SDbfu\text{-}aluF}}$
(0.950, 0.973)	(2.55, 2.755)	(2.55, 2.755)	(0.996, 0.998)	(1.117, 1.120)	(1.464, 1.482)

Then the ratio of the total diode losses after and before diode alu OC fault is

$$K_{\mathrm{TD-aluF}} = P_{\mathrm{TD-aluF}} / P_{\mathrm{TD-NOR}}. \quad (28)$$

According to (22), (24), (26), and (28), these ratios under the different diode OC faults are related to the load current I_{d}, the threshold voltage V_{T}, and slope resistance R_{s}. However, the parameters V_{T} and R_{s} are determined once diodes are selected. As a result, these ratios only depend on the load current I_{d}. Considering the different power levels of ATRUs and thus assuming that the range of load current I_{d} is (0, $+\infty$), then the range of these ratios can be easily calculated, as shown in Table I. It can be found from Table I that the total diode losses decrease slightly under single-diode OC fault. However, the losses of some diodes greatly increase compared to the normal condition. Especially, the losses of the diodes bfu and blu under diode bu OC fault are more than 2.55 times that of the normal operation, which will lead to their serious heating.

2) Winding Losses: According to Fig. 2, the total winding losses of the phase-shifting transformer can be expressed as

$$P_{\mathrm{TW}} = \sum_{X=\mathrm{A,B,C}} [I^2_{X1\mathrm{RMS}}(R_{X\mathrm{s}1} + R_{X\mathrm{s}2}) + I^2_{X2\mathrm{RMS}} R_{X\mathrm{p}} + I^2_{X3\mathrm{RMS}}(R_{X\mathrm{s}3} + R_{X\mathrm{s}4})] \quad (29)$$

where $I_{X1\mathrm{RMS}}$, $I_{X2\mathrm{RMS}}$, and $I_{X3\mathrm{RMS}}$ (X = A, B, C) are RMS values of the winding current i_{X1}, i_{X2}, and i_{X3}, and $R_{X\mathrm{s}y}$ and $R_{X\mathrm{p}}$ ($y = 1, 2, 3, 4$) are the resistance of the windings $N_{X\mathrm{s}y}$ and $N_{X\mathrm{p}}$, respectively. Considering the following relationship

$$R = \rho L / S \quad (30)$$

where ρ, L, and S are the resistivity, length, and sectional area of the winding, respectively. Thus, (29) can be rewritten as

$$P_{\mathrm{TW}} = \sum_{X=\mathrm{A,B,C}} \rho J [I_{X1\mathrm{RMS}}(L_{X\mathrm{s}1} + L_{X\mathrm{s}2}) + I_{X2\mathrm{RMS}} L_{X\mathrm{p}} + I_{X3\mathrm{RMS}}(L_{X\mathrm{s}3} + L_{X\mathrm{s}4})] \quad (31)$$

where $J = I/S$ is the winding current density set at the design stage, and $L_{X\mathrm{s}y}$ and $L_{X\mathrm{p}}$ are the length of the windings $N_{X\mathrm{s}y}$ and $N_{X\mathrm{p}}$, respectively. In fact, the windings with the same subscript for the different phases are wound on the same layer of three iron core columns, therefore their length is the same. As a result, (31) can be further simplified as

$$P_{\mathrm{TW}} = \sum_{X=\mathrm{A,B,C}} \rho J [I_{X1\mathrm{RMS}}(L_{\mathrm{As}1} + L_{\mathrm{As}2}) + I_{X2\mathrm{RMS}} L_{\mathrm{Ap}} + I_{X3\mathrm{RMS}}(L_{\mathrm{As}3} + L_{\mathrm{As}4})]. \quad (32)$$

Considering the turns ratio relation among the windings and ignoring the length difference between inner and outer windings

with the same number of turns (such as $N_{\mathrm{As1}} = N_{\mathrm{As4}}$, $N_{\mathrm{As2}} = N_{\mathrm{As3}}$) on the iron core columns, (32) can be rewritten as

$$\begin{aligned} P_{\mathrm{TW}} &= \sum_{X=\mathrm{A,B,C}} \rho J \left[(I_{X1\mathrm{RMS}} + I_{X3\mathrm{RMS}})(L_{\mathrm{As1}} + L_{\mathrm{As2}}) \right. \\ &\quad \left. + I_{X2\mathrm{RMS}} L_{\mathrm{Ap}}\right] \\ &= \sum_{X=\mathrm{A,B,C}} \rho J L_{\mathrm{As1}} \left[(I_{X1\mathrm{RMS}} + I_{X3\mathrm{RMS}})(1+\mathrm{p}) + \mathrm{q} I_{X2}\right] \end{aligned} \tag{33}$$

where $p = 0.5324$ and $q = 1.345$ are the turns ratio of the windings N_{As2} and N_{Ap} to N_{As1}, respectively. Therefore, the ratio of total winding losses after and before diode OC fault can be expressed as

$$K_{\mathrm{TW}} = \frac{\sum\limits_{X=\mathrm{A,B,C}} \left[(1+\mathrm{p})(I'_{X1\mathrm{RMS}} + I'_{X3\mathrm{RMS}}) + \mathrm{q} I'_{X2\mathrm{RMS}}\right]}{\sum\limits_{X=\mathrm{A,B,C}} \left[(1+\mathrm{p})(I_{X1\mathrm{RMS}} + I_{X3\mathrm{RMS}}) + \mathrm{q} I_{X2\mathrm{RMS}}\right]} \tag{34}$$

where $I'_{X1\mathrm{RMS}}$, $I'_{X2\mathrm{RMS}}$, $I'_{X3\mathrm{RMS}}$ are the winding current RMS values after diode OC fault and their values are shown in Appendix C. It can be calculated that $K_{\mathrm{TW}} = 0.9744$ under diode alu OC fault and $K_{\mathrm{TW}} = 1.0872$ under diode bu OC fault. Through the above analysis, the diode OC fault in ARB reduces the total winding losses slightly, while the diode OC fault in MRB increases the total winding losses by 8.72%. Furthermore, as mentioned in Section III-C, the losses in windings N_{Ap} and N_{Bp} under diode bu OC fault increase 22% due to the current 0.1049 times increased. More seriously, the losses in windings N_{As3}, N_{As4}, N_{Bs1}, and N_{Bs2} under diode bu OC fault become 1.726 times that of the normal operation. These windings are heated unevenly, potentially reducing the insulation strength of the winding and increasing the risk of a short-circuit during long-term operation.

IV. Input OC Fault Analysis of DP 18-Pulse ATRU

Input OC fault is another typical OC fault for ATRUs. In this section, the operating characteristics of DP 18-pulse ATRU under the input OC fault are explored and its influences on the aforementioned five aspects are analyzed. Here the input phase A OC fault is taken as an example.

Under phase A OC fault, only phases B and C send electricity to the load. According to the configuration of the phase-shifting transformer and Kirchhoff's voltage law, it can be derived that the relationship of the line-to-line voltages among the terminals a, b, and c of the transformer meets

$$v_{\mathrm{bc}} = 2v_{\mathrm{ba}} = 2v_{\mathrm{ac}}. \tag{35}$$

According to Fig. 1, the voltage across each winding can be expressed as

$$\begin{cases} v_{\mathrm{a'a}} = -v_{\mathrm{b''b}} = N_{\mathrm{As1}} v_{\mathrm{ba}}/\sqrt{3} \\ v_{\mathrm{b'b}} = -v_{\mathrm{c''c}} = N_{\mathrm{As1}} v_{\mathrm{cb}}/\sqrt{3} \\ v_{\mathrm{c'c}} = -v_{\mathrm{a''a}} = N_{\mathrm{As1}} v_{\mathrm{ac}}/\sqrt{3} \end{cases},$$

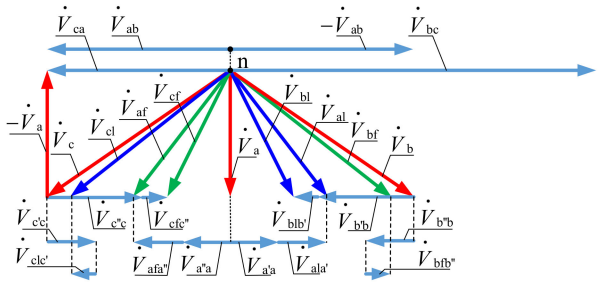

Fig. 10. Phasor diagram of the voltages of 9 terminals for the phase-shifting transformer under the input phase A OC fault.

$$\begin{cases} v_{\mathrm{ala'}} = -v_{\mathrm{afa''}} = N_{\mathrm{As2}} v_{\mathrm{bc}}/\sqrt{3} \\ v_{\mathrm{bfb''}} = -v_{\mathrm{blb'}} = N_{\mathrm{As2}} v_{\mathrm{ac}}/\sqrt{3} \\ v_{\mathrm{cfc''}} = -v_{\mathrm{clc'}} = N_{\mathrm{As2}} v_{\mathrm{ba}}/\sqrt{3} \end{cases}. \tag{36}$$

Consequently, the voltages of the output terminals for the transformer can be calculated as

$$\begin{cases} v_{\mathrm{al}} = v_{\mathrm{a}} + v_{\mathrm{a'a}} + v_{\mathrm{ala'}} \\ v_{\mathrm{bl}} = v_{\mathrm{b}} + v_{\mathrm{b'b}} + v_{\mathrm{blb'}} \\ v_{\mathrm{cl}} = v_{\mathrm{c}} + v_{\mathrm{c'c}} + v_{\mathrm{clc'}} \end{cases}, \quad \begin{cases} v_{\mathrm{af}} = v_{\mathrm{a}} + v_{\mathrm{a''a}} + v_{\mathrm{afa''}} \\ v_{\mathrm{bf}} = v_{\mathrm{b}} + v_{\mathrm{b''b}} + v_{\mathrm{bfb''}} \\ v_{\mathrm{cf}} = v_{\mathrm{c}} + v_{\mathrm{c''c}} + v_{\mathrm{cfc''}} \end{cases}. \tag{37}$$

Fig. 10 shows the phasor diagram of the phase-shifting transformer under phase A OC fault. It is perceived from Fig. 10 that the voltage v_{bc} between the terminals b and c is always maximal among the line-to-line voltages of the arbitrary two terminals. According to the principle of the uncontrolled rectifier, only four diodes connected to bridge arms b and c operate while other diodes are kept off due to the reverse bias. Consequently, this 18-pulse rectifier is weakened to a single-phase full-bridge rectifier with 2-pulse.

Furthermore, the aforementioned five aspects are analyzed under input OC fault as follows.

1) For diode conduction angle, only the voltages v_{bc} and v_{cb} are output to the dc side under phase A OC fault. Then the switching functions of bridge arms b and c can be expressed as

$$S_{\mathrm{b}} = \begin{cases} 1 \ \omega t \in [0,\pi) \\ -1 \ \omega t \in [\pi, 2\pi) \end{cases} \tag{38}$$

$$S_{\mathrm{c}} = \begin{cases} -1 \ \omega t \in [0,\pi) \\ 1 \ \omega t \in [\pi, 2\pi) \end{cases}. \tag{39}$$

According to (38) and (39), the conduction angle of the diodes bu, bd, cu, and cd changes from 80° to 180°.

2) For output voltage ripple, according to 1), it is the peak value of the voltage v_{bc} and can be expressed as

$$V_{\mathrm{R-inF}} = \sqrt{2} V_{\mathrm{bc}} \approx 2.4495\, V. \tag{40}$$

3) For transformer winding current, due to the direct connection of grid three-phase voltage and MRB's three-phase input, the transformer winding current only contains a small excitation current.
4) For input line current, it is easy to know that phases B and C input current are almost sine waves, while phase A current is zero. In high power applications, this will cause a serious unbalance of three-phase current in the front-end

of the equipment, further resulting in three-phase voltage unbalance.

5) For diode and winding losses, the current average value ($I_{\mathrm{buAV\text{-}inF}}$, $I_{\mathrm{bdAV\text{-}inF}}$, $I_{\mathrm{cuAV\text{-}inF}}$, $I_{\mathrm{cdAV\text{-}inF}}$) and RMS value ($I_{\mathrm{buRMS\text{-}inF}}$, $I_{\mathrm{bdRMS\text{-}inF}}$, $I_{\mathrm{cuRMS\text{-}inF}}$, $I_{\mathrm{cdRMS\text{-}inF}}$) through diodes bu, bd, cu, and cd are derived in Appendix A. Therefore, the single and total diode losses can be calculated as

$$\begin{aligned} P_{\mathrm{SD-inF}} &= V_{\mathrm{T}} I_{\mathrm{buAV-inF}} + I_{\mathrm{buRMS-inF}}^2 R_{\mathrm{s}} \\ &= V_{\mathrm{T}} I_{\mathrm{d}}/\pi + I_{\mathrm{d}}^2 R_{\mathrm{s}}/4 \\ P_{\mathrm{TD-inF}} &= 4P_{\mathrm{SD-inF}} = 4V_{\mathrm{T}} I_{\mathrm{d}}/\pi + I_{\mathrm{d}}^2 R_{\mathrm{s}}. \end{aligned} \tag{41}$$

The ratio of the single and total diode losses after and before input phase A fault can be respectively calculated as

$$\begin{aligned} K_{\mathrm{SD-inF}} &= P_{\mathrm{SD-inF}}/P_{\mathrm{SDMRB}} \\ K_{\mathrm{TD-inF}} &= P_{\mathrm{TD-inF}}/P_{\mathrm{TD-NOR}}. \end{aligned} \tag{42}$$

From (19), (41) and (42), the range of $K_{\mathrm{SD\text{-}inF}}$ and $K_{\mathrm{TD\text{-}inF}}$ is determined as (1.125, 1.432) and (0.5, 0.637), respectively. Therefore, the total diode losses under the input OC fault become about half of the normal operation. However, the losses of some diodes in MRB under input phase A OC fault increase significantly, which causes these diodes to suffer from serious heating stress.

Moreover, it can be known from 3) that in the case of the input OC fault, only iron losses are produced in the transformer and the winding losses are negligible.

The above analysis for phase A OC fault can also be applied to phase B or C OC fault, and similar conclusions can be obtained.

V. Discussion on OC Fault Diagnosis and Predictive Maintenance

It can be known from Sections III and IV that the diode and input OC faults extremely worsen the electrical performance of ATRU. Hence, an alert should be given immediately when the fault occurs. Naturally, the diagnosis of two types of faults is crucial. In this section, a fault diagnosis idea dealing with two types of OC faults is discussed.

This diagnosis idea contains three steps: selecting the fault feature, detecting the faults, as well as recognizing fault types and locating them. The details are as follows.

Selecting fault feature: As analyzed in Sections III and IV, the input line current, the winding current, the input current of the rectifier bridges, and the output voltage are all affected when the diode or input is open. Apparently, the realization of fault diagnosis by current monitoring is relatively cumbersome due to using more current sensors or the complicated calculation. However, the affected intervals of the output voltage caused by two types of OC faults are a significant fault feature, which can be employed to develop a fault diagnosis scheme.

Detecting faults: As shown in Fig. 4, taking the positive maximum point of input phase A voltage as the start point of dc output voltage for one period, the whole period of the dc output voltage is divided into 18 intervals equally, namely P_1, P_2, …, P_{18}. According to Sections III and IV, the affected intervals for the different diode faults and the unaffected intervals for the different input phase faults are different, which are concluded in Tables II and III, respectively. For example, the affected intervals are P_5, P_6, P_7, and P_8 (i.e., $\omega t \in [4\pi/9, 8\pi/9)$) under the diode bu fault, and the unaffected intervals are P_5 and P_{14}, (i.e., $\omega t \in [4\pi/9, 5\pi/9)$ and $\omega t \in [13\pi/9, 14\pi/9)$) under the input phase A fault. To detect the affected and unaffected intervals of one period of the dc output voltage, the 18 ratio values of the difference between the maximum value in the whole period and the minimum value in each interval to the normal output voltage ripple $V_{\mathrm{R\text{-}NOR}}$ are calculated, marked as K_1, K_{12}, …, K_{18}. According to (13) and (17) and considering the nonideal turns ratio and the leakage inductance of the transformer, when K_i ($i = 1, \ldots, 18$) is greater than 1.5, the interval P_i ($i = 1, \ldots, 18$) is affected, and the fault occurs.

TABLE II
Affected Intervals for Output Voltage Under the Different Diode OC Faults

Faulty Diode	Affected Intervals	Faulty Diode	Affected Intervals	Faulty diode	Affected Intervals
au	P_1, P_2, P_{17}, P_{18}	alu	P_3	afu	P_{16}
ad	P_8, P_9, P_{10}, P_{11}	ald	P_{12}	afd	P_7
bu	P_5, P_6, P_7, P_8	blu	P_9	bfu	P_4
bd	P_{14}, P_{15}, P_{16}, P_{17}	bld	P_{18}	bfd	P_{13}
cu	P_{11}, P_{12}, P_{13}, P_{14}	clu	P_{15}	cfu	P_{10}
cd	P_2, P_3, P_4, P_5	cld	P_6	cfd	P_1

TABLE III
Unaffected Intervals for Output Voltage Under the Different Input OC Faults

Input OC Fault	Unaffected Intervals
Phase A	P_5, P_{14}
Phase B	P_2, P_{11}
Phase C	P_8, P_{17}

Recognizing fault types and locating faults: By comparing Tables II and III, it can be found that the number of the intervals affected by input OC fault is far greater than that affected by single-diode OC fault, which can be used to recognize fault types due to the low possibility of simultaneous OC faults of multiple diodes in practice. For example, when the number of the affected intervals is more than 10, the input OC fault occurs. Otherwise, the diode OC fault occurs. Then according to the specific affected or unaffected intervals in Tables II and III, the fault location can be determined.

Moreover, in addition to repairing the fault objects after locating the fault, the predictive maintenance objects should also be concerned. As mentioned in Sections III and IV, the diode OC faults in MRB and input OC faults lead to a great increase in the losses of some diodes and windings, which are summarized in Table IV. These diodes and windings should be predictively maintained.

VI. Simulation and Experimental Results

In order to verify the effectiveness and correctness of the theoretical analysis in Sections II–V, under the limit of the

TABLE IV
PREDICTIVE MAINTENANCE OBJECTS AFTER FAULT DIAGNOSIS

Faulty Object	Predictive Maintenance Objects	Faulty Object	Predictive Maintenance Objects
au	Diodes: afu, alu Windings: N_{As1}, N_{As2}, N_{Cs3}, N_{Cs4}	ad	Diodes: afd, ald Windings: N_{As1}, N_{As2}, N_{Cs3}, N_{Cs4}
bu	Diodes: bfu, blu Windings: N_{As3}, N_{As4}, N_{Bs1}, N_{Bs2}	bd	Diodes: bfd, bld Windings: N_{As3}, N_{As4}, N_{Bs1}, N_{Bs2}
cu	Diodes: cfu, clu Windings: N_{Cs1}, N_{Cs2}, N_{Bs3}, N_{Bs4}	cd	Diodes: cfd, cld Windings: N_{Cs1}, N_{Cs2}, N_{Bs3}, N_{Bs4}
Phase A	Diodes: bu, bd, cu, cd	Phase B	Diodes: au, ad, cu, cd
Phase C	Diodes: au, ad, bu, bd		

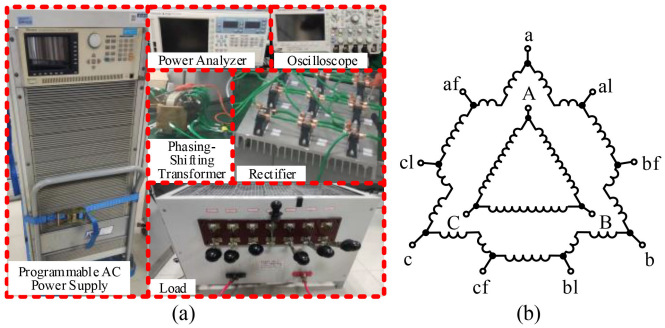

Fig. 11. Experimental platform of the asymmetric DP transformer rectifier unit. (a) Configuration of the platform. (b) Winding configuration of the phase-shifting transformer used in the simulation model and experimental platform.

TABLE V
SYSTEM PARAMETERS

Parameters	Values	Parameters	Values
Power: P	1.4 kW	Frequency: f	400 Hz
Grid voltage	115 V	Step-down ratio	10
DC voltage: V_{DC}	28 V	Load: R_L	0.6 Ω

experimental condition, an experimental platform of the asymmetric step-down DP 18-pulse transformer rectifier unit is established, as shown in Fig. 11(a). The winding structure of the isolated phase-shifting transformer is shown in Fig. 11(b). It is worth noting that the primary delta-connected windings ABC in Fig. 11(b) are only for realizing step-down and galvanic isolation, which does not affect the verification of the mentioned theory analysis except for the losses. The system parameters are given in Table V.

A. Normal Operation

Fig. 12(a) and (b) gives the simulation and experimental results of three-phase input current under normal operation. It can be clearly observed that each of them has 18 steps and is nearly sinusoidal. Fig. 13 shows the spectrum of the three-phase input current in the experimental waveforms. Compared to the theoretical results in Fig. 9(a), the noncharacteristic harmonic components appear in the three-phase input current. The reason is that the nonideal turns ratio of the transformer caused by the inevitable deviation of winding turns between the designed noninteger value and manufactured integer value weakens the

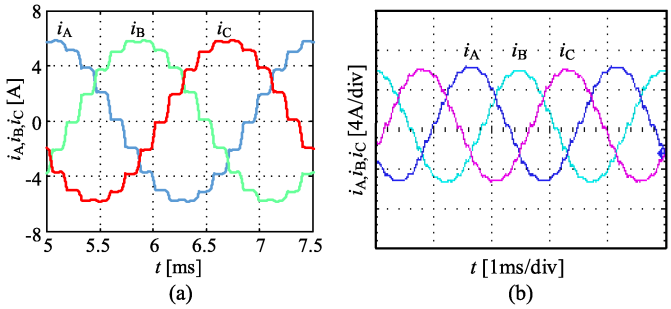

Fig. 12. Simulation and experimental results of the three-phase input current under normal operation. (a) Simulation result. (b) Experimental result.

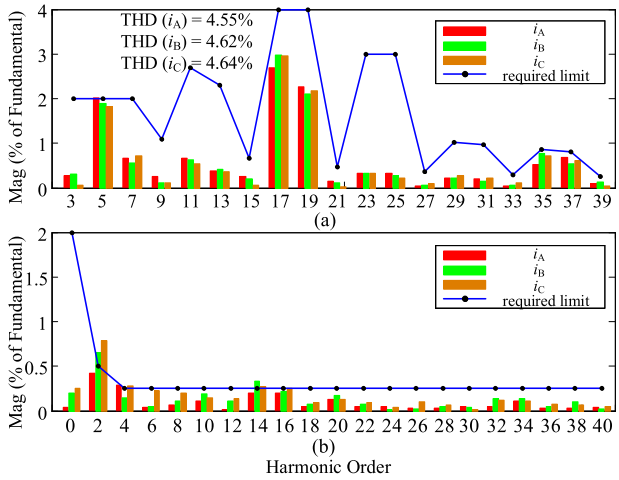

Fig. 13. Spectrum of three-phase input current in the experimental waveforms under normal operation. (a) Odd harmonics. (b) Even harmonics.

cancellation of these non-characteristic harmonics, which was explained in detail in [25]. Moreover, the current THD value of experimental results (about 4.6%) is better than the theoretical value (10.1%). On the one hand, the leakage inductance leads to the commutation overlap angle, which makes the current flowing through the diode close to a trapezoidal wave rather than a rectangular wave, improving the sinusoidal degree of the input current [26]. On the other hand, from the perspective of the filter, the leakage inductance of the transformer has a good damping effect on the harmonic components due to the high power frequency [25]. Thus, the input current has a lower THD compared to the theoretical analysis. It is clear that the majority of individual frequency components do not exceed the ISO 1540 and DO-160F requirements.

Fig. 14 illustrates the simulation and experimental results of the dc output voltage under normal operation. As can be seen, the dc output voltage has 18 wave crests in one period, which is consistent with the theoretical analysis. However, the output voltage ripple in the experimental result is about 1.3 V, which is higher than the theoretical value. There are two main reasons. One is that the nonideal turns ratio of the transformer results in the different peak values of the 18 line-to-line voltages transmitted to the dc side, increasing the output voltage ripple [25]. The other is that the commutation voltage drop is generated due to the leakage inductance of the transformer, further increasing

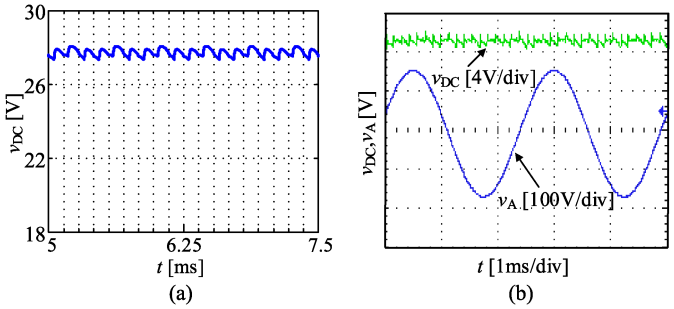

Fig. 14. Simulation and experimental results of dc output voltage under normal operation. (a) Simulation result. (b) Experimental result.

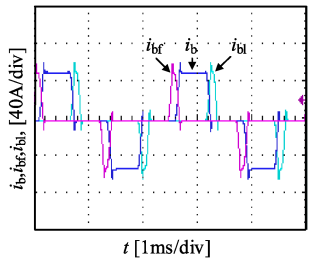

Fig. 15. Experimental results of input current i_b, i_{bl}, and i_{bf} of the rectifier bridge under normal operation.

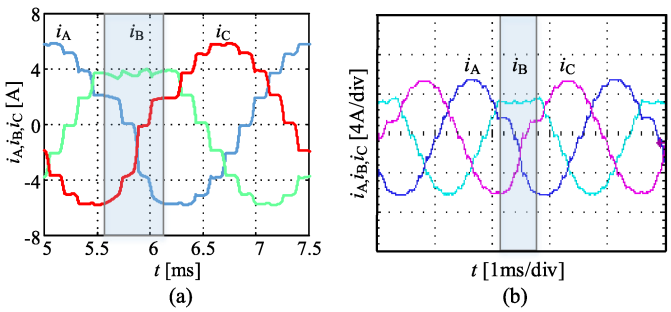

Fig. 16. Simulation and experimental results of the three-phase input current under the diode bu OC fault. (a) Simulation result. (b) Experimental result.

the output voltage ripple [27], [28]. Fig. 15 shows experimental results of the input currents i_b, i_{bf}, and i_{bl} of the rectifier bridge under normal operation. It can be found that the diodes bfu and blu conduct ahead and behind diode bu, respectively. Moreover, the conduction angle of diodes bu and bd in MRB is about 4 times that of diodes blu, bld, bfu, and bfd in ARB, which verifies the theoretical analysis in Section II.

B. Diode Bu OC Fault in MRB

Fig. 16 presents the simulation and experimental waveforms of the three-phase input current under diode bu OC fault. It is worth noting that the fifth millisecond in the simulation result corresponds to the positive maximal point of phase A voltage. From Fig. 16(a), the three-phase input current is only disturbed between 5.56 ms and 6.11 ms (i.e., $\omega t \in [4\pi/9, 8\pi/9)$), and the current symmetry is severely destroyed. The wave crest of phase B current in the positive half-cycle is cut off, which introduces high dc components into the ac system. The same phenomenon

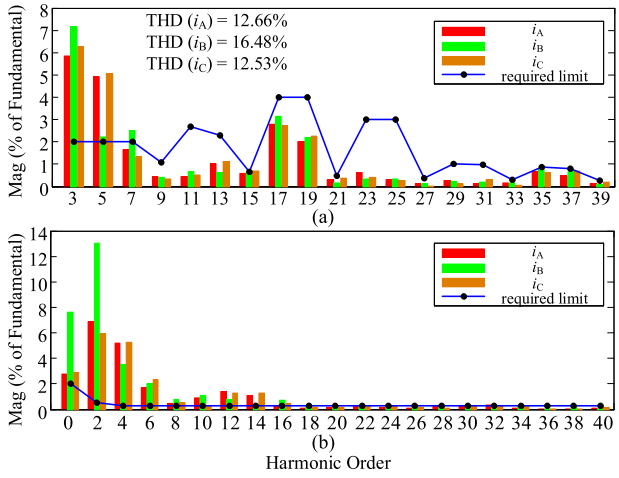

Fig. 17. Spectrum of three-phase input current in the experimental waveforms under the diode bu OC fault. (a) Odd harmonics. (b) Even harmonics.

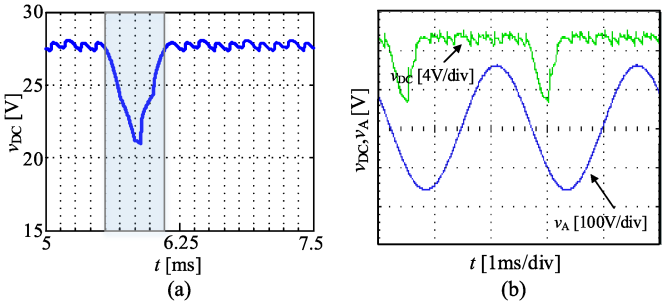

Fig. 18. Simulation and experimental results of the dc output voltage under the bu OC fault. (a) Simulation result. (b) Experimental result.

can be found in Fig. 16(b). Fig. 17 gives the spectrum of the three-phase input current in experimental waveforms. The dc components with different contents can be found in the three-phase current. Especially in phase B current, the content is up to 7.6%. The harmonics are mainly distributed in 2nd—7th, 17th, 19th, 35th, and 37th. Importantly, the contents for the 2nd–6th harmonics greatly exceed the requirements in the standard ISO 1540. In addition, the THD values of the three-phase input current are 12.66%, 16.48%, and 12.53%, respectively, which are much higher than the normal operation and higher than the requirement (i.e., 10%).

In Fig. 18, the sags with 80° appear in the output voltage due to the diode bu OC fault. As can be seen, the sag only occurs between 5.56 and 6.11 ms (i.e., intervals P_5, P_6, P_7, and P_8) and the output voltage ripple in Fig. 18(b) is about 6.7 V, which can be used to judge the diode bu OC fault according to Table II. Fig. 19 shows the experimental results of the sags that consist of the different parts of the four line-to-line voltages v_{bfc}, v_{bfcl}, v_{blaf}, and v_{bla}, which corresponds to the theoretical analysis.

Fig. 20 presents the experimental results of the affected input current of the rectifier bridge under bu OC fault. As can be seen, the positive half-cycle of the current i_b disappears due to the diode bu OC fault. In addition, compared with the normal condition shown in Fig. 15, the pulse width of the positive half-cycle of the currents i_{bf} and i_{bl} increases but is less than the

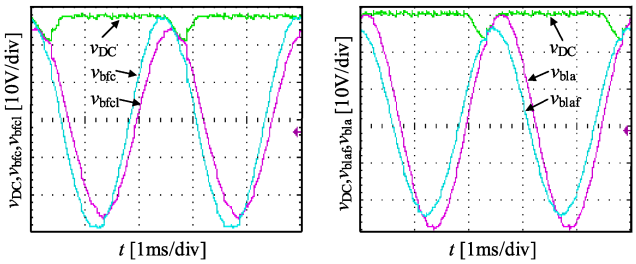

Fig. 19. Verification results of the composition of the sag in the output voltage under the diode bu OC fault.

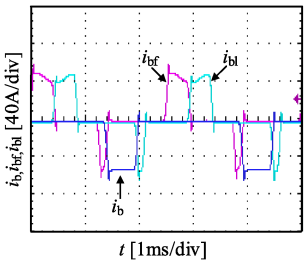

Fig. 20. Experimental result of input current i_b, i_{bf}, i_{bl} for the rectifier bridge under the diode bu OC fault.

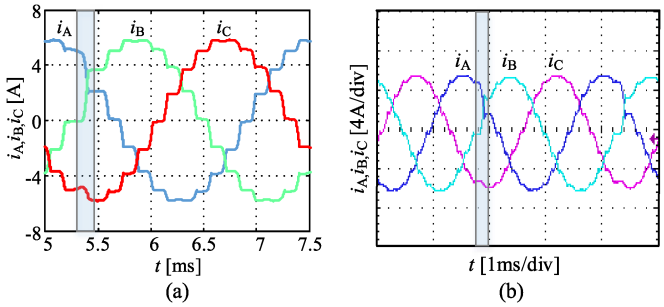

Fig. 21. Simulation and experimental results of three-phase input current under the diode alu OC fault. (a) Simulation result. (b) Experimental result.

pulsewidth of the diode in the MRB, which reveals the working mechanism under the diode OC fault.

C. Diode Alu OC Fault in ARB

In Fig. 21(a), the three-phase input current is only disturbed from 5.28 to 5.42 ms (i.e., $\omega t \in [2\pi/9, \pi/3)$) under diode alu OC fault, and this disturbance is obviously slight compared to diode bu OC fault. The same phenomenon is also observed in Fig. 21(b). According to the spectrum for the experimental three-phase input current in Fig. 22, harmonics are mainly distributed in 2nd–24th, 35th, and 37th. Among them, the 5th, 7th, 9th, 15th, and 21st odd harmonic components slightly exceed the requirements. However, a large number of even harmonics (2nd, 4th, …, 26th) are higher than the required limit of ISO 1540. Moreover, although THD values (7.16%, 7.5%, 5.32%) of three-phase input current increase compared to the normal operation, they still meet the required limit.

In Fig. 23, the position of the sags in the output voltage is at the interval $\omega t \in [2\pi/9, \pi/3)$ and the output voltage ripple (2.6 V) in Fig. 23(b) is obviously higher than the normal value, which can

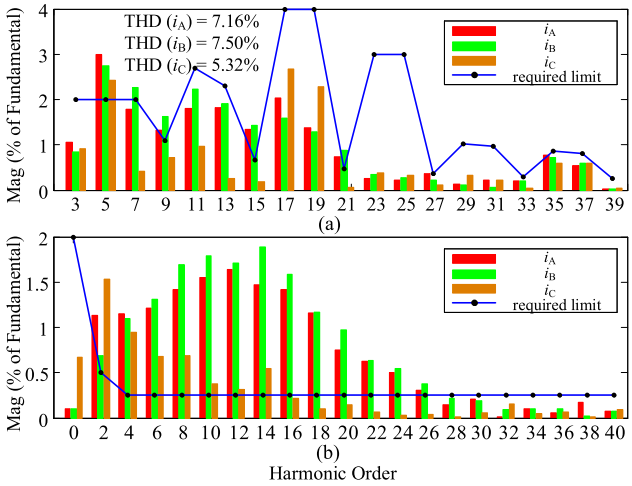

Fig. 22. Spectrum of three-phase input current in the experimental waveforms under the diode alu OC fault. (a) Odd harmonics. (b) Even harmonics.

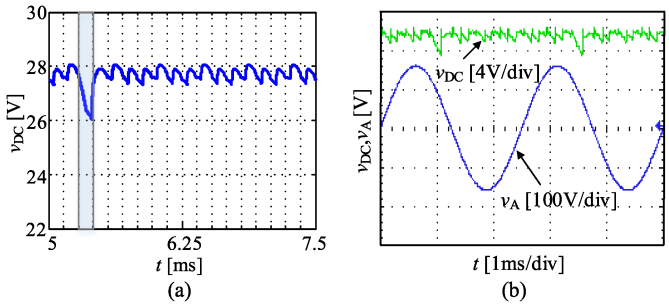

Fig. 23. Simulation and experimental results of dc output voltage under the diode alu OC fault. (a) Simulation result. (b) Experimental result.

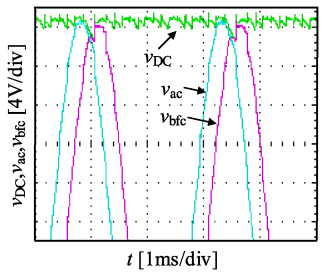

Fig. 24. Verification results of the composition of the sag in the output voltage under the diode alu OC fault.

determine the faulty diode alu according to Table II. Moreover, from Fig. 24, the composition of the sag caused by the diode alu OC fault is also verified. In Fig. 25, due to the diode alu OC fault, the positive half-cycle of the current i_{al} disappears, and the pulsewidth of the positive half-cycle of the current i_a and i_{bf} increases 10°, respectively. In a word, the above conclusions are consistent with the theoretical analysis.

D. Input Phase A OC Fault

Fig. 26 shows the experimental result of voltage waveforms of three terminals a, b, and c for the secondary side of the isolated transformer under the input phase A OC fault. It can be clearly observed that the voltages of the terminals b and c are the same

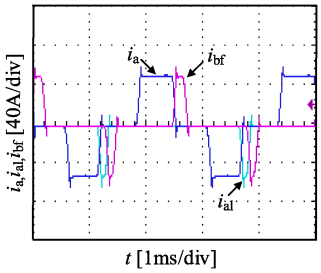

Fig. 25. Experimental results of the input current $i_{\rm a}$, $i_{\rm al}$, $i_{\rm bf}$ of the rectifier bridge.

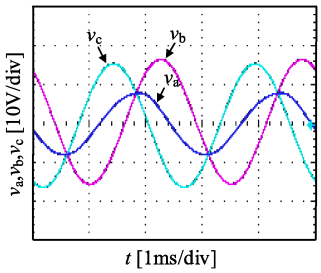

Fig. 26. Experimental result of the three terminal voltages of transformer secondary side under the input phase A OC fault.

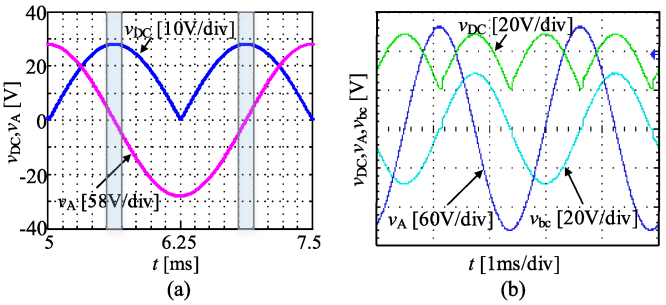

Fig. 27. Simulation and experimental results of dc output voltage under input phase A OC fault. (a) Simulation result. (b) Experimental result.

as the normal condition, while the amplitude of the terminal a voltage becomes half of the normal operation and its phase is 60° ahead of the terminal c voltage, which strictly corresponds to the theoretical analysis.

Fig. 27 presents the simulation and experimental results of the voltage $v_{\rm bc}$, grid voltage $v_{\rm A}$, and output voltage $v_{\rm DC}$ under the input phase A OC fault. It is clear that the frequency of the output voltage is doubled compared to the supply frequency. The waveform of the output voltage is exactly the same as the positive half-wave of the voltages $v_{\rm bc}$ and $v_{\rm cb}$, which verifies that only voltages $v_{\rm bc}$ and $v_{\rm cb}$ are output to the dc side. Meanwhile, the output voltage ripple is the peak value of the voltage $v_{\rm bc}$. Moreover, the unaffected interval of the dc output voltage is 5.56–5.69 ms and 6.81–6.94 ms (i.e., intervals P_5 and P_{14}). According to Table III, the input phase A OC fault can be identified.

In Fig. 28, the experimental waveforms of the bridge arms current and input current under phase A OC fault are given. As can be seen, the waveforms of the input line current have good sinusoidal features, only slight distortion appears at the

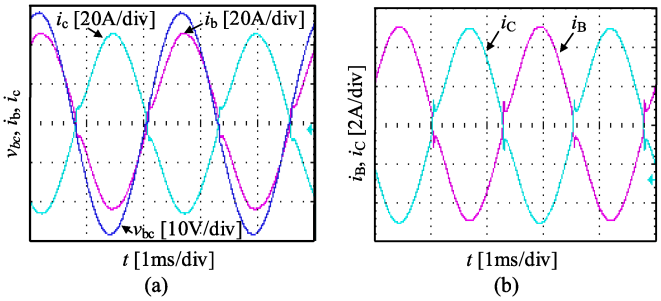

Fig. 28. Experimental waveforms of the bridge arms current and input current under the phase A OC fault. (a) Current of the bridge arms b and c. (b) Input current of phases B and C.

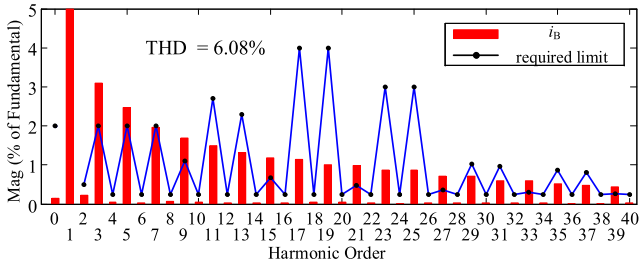

Fig. 29. Spectrum of the input phase B current in the experimental waveforms under input phase A OC fault.

TABLE VI
COMPARISON OF OTHER ELECTRICAL INDICES UNDER THE DIFFERENT CASES

Case	Input active power (kW)	Output active power (kW)	Effici-ency	Input reactive power (kVar)	Power factor (PF)		
					Phase A	Phase B	Phase C
1	1.373	1.180	85.94%	0.156	0.993	0.994	0.994
2	1.310	1.112	84.89%	0.328	0.966	0.955	0.984
3	1.366	1.173	85.87%	0.175	0.992	0.991	0.993
4	0.675	0.573	84.89%	0.098	/	0.927	0.781

Case 1: normal operation. Case 2: diode bu OC fault. Case 3: diode alu OC fault. Case 4: input phase A OC fault.

zero-crossing point due to the current commutation. Fig. 29 shows the spectrum of phase B input current, it can be seen that the THD value of the input current increases slightly compared to 4.6% for the normal operation. Meanwhile, the three-phase input current is severely unbalanced since the phase A current is zero, which should be avoided in practice. It should be pointed out that the winding current of the transformer in the experimental platform contains load current under the input phase A OC fault because energy is transmitted by the magnetic field due to the galvanic isolation of primary and secondary windings. Nevertheless, this phenomenon does not affect the effectiveness of verification except for the losses.

E. Other Electrical Performance Indices Under OC Fault

Table VI shows the comparison of other electrical performance indices under the normal operation and different fault cases. From Table VI, the efficiency of the 18-pulse transformer rectifier unit is obviously lower than that (≥97% [15]) of the

TABLE VII
NORMALIZED INDEX VALUE OF THE OBJECT THAT NEGATIVE INFLUENCES THE CORRESPONDING INDEX MOST UNDER THE DIFFERENT OC FAULTS

Operation modes	Diode conduction angle		Output voltage ripple	Single-winding current RMS	Single input line current THD	Single-diode losses		Single-winding losses	Total winding losses
	Diode in MRB	Diode in ARB				Diode in MRB	Diode in ARB		
Normal operation	1.000	1.000	1.000	1.000	1.000	1.000	1.000	1.000	1.000
Diode bu OC fault	/	3.000	15.715	1.314	1.824	/	2.755	1.726	1.087
Diode alu OC fault	1.125	1.500	3.970	1.061	1.226	1.120	1.482	1.126	/
Input phase A OC fault	2.250	/	65.847	/	/	1.432	/	/	/

common ATRUs due to the phase-shifting transformer with galvanic isolation in the experimental platform. Three conclusions can be summarized as follows.

Single-diode and single-input OC faults have little effect on the efficiency of the converter.

In the normal operation, there is extremely high PF on the input side. However, the PF on the input side decreases when diode OC fault occurs, which makes more reactive power need to be supplied, increasing the burden of the power source. In addition, the input OC fault leads to the PF decreasing seriously, while only less reactive power on the input side. The reason is that the reactive power for capacitive in phase B and inductive in phase C is neutralized inside the converter.

The OC fault results in a decrease in the output power of the converter. Especially, the output power will become half of the normal operation under the input OC fault, which greatly weakens its feeding capacity.

VII. CONCLUSION

First, this article comprehensively analyzed the influences of diode and input OC faults of the asymmetric DP 18-pulse ATRU on the five aspects: diode conduction angle, output voltage ripple, winding current, input current harmonics, and losses of diode and winding. Table VII gives the theoretical index value (Normalized value according to the normal operation) of the object that negatively influences the corresponding index most under the different OC faults. Compared to the diode OC fault in ARB, the diode OC fault in MRB has a more significant impact on the above five aspects. Especially, the output voltage ripple and the THD of the input current seriously exceed the requirements in related standards under the diode fault in MRB. Moreover, ATRU is weakened to be a single-phase rectifier under the input OC fault, which results in a great increase in the losses of the diode in MRB and the output voltage ripple, and a serious unbalance of the input current. Second, based on the number and position of the affected intervals of the output voltage caused by the different diode and input OC faults, a fault diagnosis method coping with two types of OC faults was developed. Meanwhile, based on the loss analysis, those diodes and windings that should be predictively maintained after locating the fault were also summarized. Finally, simulation and experimental results confirmed the correctness of the analysis and discussions. This work not only clarifies the harm of OC fault but also is beneficial to developing fault diagnosis schemes and digging predictive maintenance objects. In addition, the analysis framework and approach of this article can be easily applied to other multipulse rectifiers.

APPENDIX A

1) Under normal operation, each diode in MRB and ARB conducts 80° and 20°, respectively. Therefore, the current average value and RMS value through each diode in MRB and ARB can be calculated respectively

$$\begin{cases} I_{\mathrm{MRBAV}} = 4I_{\mathrm{d}}/18 \\ I_{\mathrm{ARBAV}} = I_{\mathrm{d}}/18 \end{cases} \begin{cases} I_{\mathrm{MRBRMS}} = \sqrt{2}I_{\mathrm{d}}/3 \\ I_{\mathrm{ARBRMS}} = \sqrt{2}I_{\mathrm{d}}/6 \end{cases}. \quad \text{(A-1)}$$

2) Under the diode bu OC fault, according to Fig. 4, the symmetrical output voltage drop appears in the interval $\omega t \in [4\pi/9, 8\pi/9)$. Then the constant current values $k_{1\mathrm{AV}}$ and $k_{1\mathrm{RMS}}$ in the interval $\omega t \in [4\pi/9, 5\pi/9) \cup [7\pi/9, 8\pi/9)$ should meet (A-2) and (A-3) as per the average value equivalent and RMS value equivalent, respectively

$$\frac{1}{2\pi}\int_{\pi/18}^{3\pi/18} I_{\mathrm{d}}\cos(\omega t)d(\omega t) = \frac{1}{2\pi}\int_{\pi/18}^{3\pi/18} k_{1\mathrm{AV}}I_{\mathrm{d}}d(\omega t) \quad \text{(A-2)}$$

$$\sqrt{\frac{1}{2\pi}\int_{\pi/18}^{3\pi/18} (I_{\mathrm{d}}\cos(\omega t))^2 d(\omega t)} = \sqrt{\frac{1}{2\pi}\int_{\pi/18}^{3\pi/18} (k_{1\mathrm{RMS}}I_{\mathrm{d}})^2 d(\omega t)}. \quad \text{(A-3)}$$

Similarly, the constant current values $k_{2\mathrm{AV}}$ and $k_{2\mathrm{RMS}}$ in the interval $\omega t \in [5\pi/9, 7\pi/9)$ should meet (A-4) and (A-5) as per the average value equivalent and RMS value equivalent, respectively

$$\frac{1}{2\pi}\int_{\pi/18}^{3\pi/18} \mathrm{z}I_{\mathrm{d}}\cos(\omega t)d(\omega t) = \frac{1}{2\pi}\int_{\pi/18}^{3\pi/18} k_{2\mathrm{AV}}I_{\mathrm{d}}d(\omega t) \quad \text{(A-4)}$$

$$\sqrt{\frac{1}{2\pi}\int_{\pi/18}^{3\pi/18} (\mathrm{z}I_{\mathrm{d}}\cos(\omega t))^2 d(\omega t)} = \sqrt{\frac{1}{2\pi}\int_{\pi/18}^{3\pi/18} (k_{2\mathrm{RMS}}I_{\mathrm{d}})^2 d(\omega t)} \quad \text{(A-5)}$$

where $\mathrm{z} = V_{\mathrm{bfcl}}/V_{\mathrm{bc}} = 0.8791$. Therefore, the current average value and RMS value of the affected six diodes bfu, blu, cd, ad, cld, and afd under diode bu OC fault can be respectively calculated as (A-6)shown at the top of the next page.

$$\begin{cases} I_{\mathrm{bfuAV-buF}} = I_{\mathrm{bluAV-buF}} = (1 + k_{1\mathrm{AV}} + k_{2\mathrm{AV}})I_{\mathrm{d}}/18 \approx 0.1532I_{\mathrm{d}} \\ I_{\mathrm{cdAV-buF}} = I_{\mathrm{adAV-buF}} = (3 \times 1 + k_{1\mathrm{AV}})I_{\mathrm{d}}/18 \approx 0.2186I_{\mathrm{d}} \\ I_{\mathrm{cldAV-buF}} = I_{\mathrm{afdAV-buF}} = k_{2\mathrm{AV}}I_{\mathrm{d}}/18 \approx 0.0457I_{\mathrm{d}} \\ I_{\mathrm{bfuRMS-buF}} = I_{\mathrm{bluRMS-buF}} = \sqrt{(1^2 + k_{1\mathrm{RMS}}^2 + k_{2\mathrm{RMS}}^2)/18}I_{\mathrm{d}} \approx 0.3765I_{\mathrm{d}} \\ I_{\mathrm{cdRMS-buF}} = I_{\mathrm{adRMS-buF}} = \sqrt{(3 \times 1^2 + k_{1\mathrm{RMS}}^2)/18}I_{\mathrm{d}} \approx 0.464I_{\mathrm{d}} \\ I_{\mathrm{cldRMS-buF}} = I_{\mathrm{afdRMS-buF}} = \sqrt{k_{2\mathrm{RMS}}^2/18}I_{\mathrm{d}} \approx 0.1938I_{\mathrm{d}} \end{cases} . \tag{A-6}$$

3) Under the diode alu OC fault, according to Fig. 4, the constant current values $k_{3\mathrm{AV}}$ and $k_{3\mathrm{RMS}}$ in the interval $\omega t \in [2\pi/9, \pi/3)$ should meet (A-7) and (A-8) as per the average value equivalent and RMS value equivalent, respectively

$$\frac{1}{2\pi}\int_{\pi/18}^{\pi/9} I_{\mathrm{d}}\cos(\omega t)d(\omega t) = \frac{1}{2\pi}\int_{\pi/18}^{\pi/9} k_{3\mathrm{AV}}I_{\mathrm{d}}d(\omega t) \tag{A-7}$$

$$\sqrt{\frac{1}{2\pi}\int_{\pi/18}^{\pi/9} (I_{\mathrm{d}}\cos(\omega t))^2 d(\omega t)} = \sqrt{\frac{1}{2\pi}\int_{\pi/18}^{\pi/9} (k_{3\mathrm{RMS}}I_{\mathrm{d}})^2 d(\omega t)}. \tag{A-8}$$

Then the current average value and RMS value of the affected three diodes au, cd, and bfu under diode alu OC fault can be respectively calculated as

$$\begin{cases} I_{\mathrm{auAV-aluF}} = (8 \times 1 + k_{3\mathrm{AV}})I_{\mathrm{d}}/36 \approx 0.2489I_{\mathrm{d}} \\ I_{\mathrm{cdAV-aluF}} = (6 \times 1 + 2 \times k_{3\mathrm{AV}})I_{\mathrm{d}}/36 \approx 0.2203I_{\mathrm{d}} \\ I_{\mathrm{bfuAV-aluF}} = (2 \times 1 + k_{3\mathrm{AV}})I_{\mathrm{d}}/36 \approx 0.0824I_{\mathrm{d}} \end{cases}$$

$$\begin{cases} I_{\mathrm{auRMS-aluF}} = \sqrt{(8 \times 1^2 + k_{3\mathrm{RMS}}^2)/36}I_{\mathrm{d}} \approx 0.4981I_{\mathrm{d}} \\ I_{\mathrm{cdRMS-aluF}} = \sqrt{(6 \times 1^2 + 2 \times k_{3\mathrm{RMS}}^2)/36}I_{\mathrm{d}} \approx 0.4673I_{\mathrm{d}} \\ I_{\mathrm{bfuRMS-aluF}} = \sqrt{(2 \times 1^2 + k_{3\mathrm{RMS}}^2)/36}I_{\mathrm{d}} \approx 0.2835I_{\mathrm{d}} \end{cases} . \tag{A-9}$$

4) Under the input phase A OC fault, according to the analysis in Section IV, the current average value and RMS value through diodes bu, bd, cu, and cd are respectively equal, and they are roughly evaluated using the following equation:

$$I_{\mathrm{buAV-inF}} = \frac{1}{2\pi}\int_0^{\pi} I_{\mathrm{d}}\sin(\omega t)d(\omega t) = \frac{I_{\mathrm{d}}}{\pi}$$

$$I_{\mathrm{buRMS-inF}} = \sqrt{\frac{1}{2\pi}\int_0^{\pi} (I_{\mathrm{d}}\sin(\omega t))^2 d(\omega t)} = \frac{1}{2}I_{\mathrm{d}}. \tag{A-10}$$

APPENDIX B

Normal operation:

b_1 - b_{36}:
0, -0.3952I_{d}, -0.3952I_{d}, -0.7421I_{d}, -0.7421I_{d}, -I_{d}, -I_{d}, -1.1373I_{d}, -1.1373I_{d}, -1.1373I_{d}, -1.1373I_{d}, -I_{d}, -I_{d}, -0.7421I_{d}, -0.7421I_{d}, -0.3952I_{d}, -0.3952I_{d}, 0, 0, 0.3952I_{d}, 0.3952I_{d}, 0.7421I_{d}, 0.7421I_{d}, I_{d}, I_{d}, 1.1373I_{d}, 1.1373I_{d}, 1.1373I_{d}, 1.1373I_{d}, I_{d}, I_{d}, 0.7421I_{d}, 0.7421I_{d}, 0.3952I_{d}, 0.3952I_{d}, 0.

When the diode OC fault occurs, the changed b_i compared to the normal operation are as follows:

Diode bu OC fault:

Phase A current (i_{A}): b_1–b_7: 0.3697I_{d}, 0, 0, -0.7232I_{d}, -0.7232I_{d}, -1.0640I_{d}, -1.0640I_{d};
b_{36}: 0.3967I_{d}.
Phase B current (i_{B}): b_{24}-b_{31}: 0.6943I_{d}, 0.6943I_{d}, 0.7232I_{d}, 0.7232I_{d}, 0.7232I_{d}, 0.7232I_{d}, 0.6943I_{d}, 0.6943I_{d}.
Phase C current (i_{C}): b_{12}-b_{19}: -1.0640I_{d}, -1.0640I_{d}, -0.7232I_{d}, -0.7232I_{d}, 0, 0, 0.3697I_{d}, 0.3697I_{d}.

Diode alu OC fault:

Phase A current (i_{A}): b_{32} - b_{33}: 0.9648I_{d}, 0.3813I_{d}.
Phase B current (i_{B}): b_{20} - b_{21}: 0, 0.7160I_{d}.
Phase C current (i_{C}): b_8 - b_9: -0.9648I_{d}, -1.0973I_{d}.

APPENDIX C

Normal operation:

$I_{\mathrm{A1RMS}} = 0.2618I_{\mathrm{d}}$, $I_{\mathrm{A2RMS}} = 0.1449I_{\mathrm{d}}$, $I_{\mathrm{A3RMS}} = 0.2618I_{\mathrm{d}}$, $I_{\mathrm{B1RMS}} = 0.2618I_{\mathrm{d}}$, $I_{\mathrm{B2RMS}} = 0.1449I_{\mathrm{d}}$, $I_{\mathrm{B3RMS}} = 0.2618I_{\mathrm{d}}$, $I_{\mathrm{C1RMS}} = 0.2618I_{\mathrm{d}}$, $I_{\mathrm{C2RMS}} = 0.1449I_{\mathrm{d}}$, $I_{\mathrm{C3RMS}} = 0.2618I_{\mathrm{d}}$.

Diode bu OC fault:

$I'_{\mathrm{A1RMS}} = 0.2705I_{\mathrm{d}}$, $I'_{\mathrm{A2RMS}} = 0.1601I_{\mathrm{d}}$, $I'_{\mathrm{A3RMS}} = 0.3439I_{\mathrm{d}}$, $I'_{\mathrm{B1RMS}} = 0.3439I_{\mathrm{d}}$, $I'_{\mathrm{B2RMS}} = 0.1601I_{\mathrm{d}}$, $I'_{\mathrm{B3RMS}} = 0.2705I_{\mathrm{d}}$, $I'_{\mathrm{C1RMS}} = 0.2519I_{\mathrm{d}}$, $I'_{\mathrm{C2RMS}} = 0.1242I_{\mathrm{d}}$, $I'_{\mathrm{C3RMS}} = 0.2519I_{\mathrm{d}}$.

Diode alu OC fault:

$I'_{\mathrm{A1RMS}} = 0.2058I_{\mathrm{d}}$, $I'_{\mathrm{A2RMS}} = 0.1363I_{\mathrm{d}}$, $I'_{\mathrm{A3RMS}} = 0.2778I_{\mathrm{d}}$, $I'_{\mathrm{B1RMS}} = 0.2606I_{\mathrm{d}}$, $I'_{\mathrm{B2RMS}} = 0.1427I_{\mathrm{d}}$, $I'_{\mathrm{B3RMS}} = 0.2606I_{\mathrm{d}}$, $I'_{\mathrm{C1RMS}} = 0.2623I_{\mathrm{d}}$, $I'_{\mathrm{C2RMS}} = 0.1459I_{\mathrm{d}}$, $I'_{\mathrm{C3RMS}} = 0.2623I_{\mathrm{d}}$.

REFERENCES

[1] J. Chen et al., "Evaluation on the autoconfigured multipulse AC/DC rectifier and their application in more electric aircrafts," *IEEE Trans. Transp. Electrif.*, vol. 6, no. 4, pp. 1721–1739, Dec. 2020.

[2] B. Singh, S. Gairola, B. N. Singh, A. Chandra, and K. Al-Haddad, "Multipulse AC-DC converters for improving power quality: A review," *IEEE Trans. Power Electron.*, vol. 23, no. 1, pp. 260–281, Jan. 2008.

[3] R. Abdollahi and G. B. Gharehpetian, "A 20-Pulse autotransformer rectifier unit for more electric aircrafts," *IEEE J. Emerg. Sel. Topics. Power Electron.*, vol. 9, no. 3, pp. 2992–2999, Jun. 2021.

[4] R. Kalpana, K. S. Chethana, S. P. P., and B. Singh, "Power quality enhancement using current injection technique in a zigzag configured autotransformer-based 12-Pulse rectifier," *IEEE Trans. Ind. Appl.*, vol. 54, no. 5, pp. 5267–5277, Sep. 2018.

[5] F. Meng, L. Gao, W. Yang, and S. Yang, "Comprehensive comparison of the Delta- and Wye-connected autotransformer applied to 12-Pulse rectifier," *J. Mod. Power Syst. Clean Energy*, vol. 4, no. 1, pp. 135–145, Oct. 2016.
[6] B. Singh, V. Garg, and G. Bhuvaneswari, "A novel T-connected Autotransformer-based 18-pulse AC–DC converter for harmonic mitigation in adjustable-speed induction-motor drives," *IEEE Trans. Ind. Electron.*, vol. 54, no. 5, pp. 2500–2511, Oct. 2007.
[7] Y. Zhang, Z. Chen, B. Li, and Y. He, "Application of low-harmonic 18-Pulse rectifier power supply for radar power system," *IEEE Trans. Ind. Electron.*, vol. 66, no. 2, pp. 1080–1088, Oct. 2019.
[8] Y. Zhang, X. Zhang, Z. Chen, B. Li, and Y. He, "Engineering application research of aircraft power supply characteristics based on 18-Pulse rectifier power system," *IEEE Access*, vol. 7, pp. 22026–22034, 2019.
[9] Y. Zhang, Z. Chen, B. Li, and Y. He, "A simple harmonic reduction method in multipulse rectifier using passive devices," *IEEE Trans. Ind. Electron.*, vol. 13, no. 5, pp. 2680–2692, Oct. 2017.
[10] J. Chen, H. Bai, J. Chen, and C. Gong, "A novel parallel configured 48-Pulse autotransformer rectifier for aviation application," *IEEE Trans. Power Electron.*, vol. 37, no. 2, pp. 2125–2138, Feb. 2022.
[11] X. Lian, S. Yang, and W. Yang, "Optimum design of 48-Pulse rectifier using unconventional interphase reactor," *IEEE Access*, vol. 7, pp. 61240–61250, 2019.
[12] *Aerospace-Characteristics of Aircraft Electrical Systems*, ISO 1540, 2006.
[13] *Environmental Conditions and Test Procedures for Airborne Equipment*, Standard RTCA DO-160F, 2007.
[14] R. Burgos, A. Uan-Zo-li, F. Lacaux, F. Wang, and D. Boroyevich, "Analysis of experimental evaluation of symmetric and asymmetric 18-Pulse autotransformer rectifiers topologies," in *Proc. IEEE 36th Power Electron. Spec. Conf.*, Apr. 2007, pp. 1149–1155.
[15] J. Chen, J. Shen, J. Chen, P. Shen, Q. Song, and C. Gong, "Investigation on the selection and design of step-up/down 18-pulse ATRUs for more electric aircrafts," *IEEE Trans. Transp. Electrif.*, vol. 5, no. 3, pp. 795–811, Jul. 2019.
[16] T. Kamel, Y. Biletskiy, and L. Chang, "Real-Time diagnosis for open-circuited and unbalance faults in electronic converters connected to residential wind systems," *IEEE Trans. Ind. Electron.*, vol. 63, no. 3, pp. 1781–1792, Mar. 2016.
[17] J. S. Perisé, M. Baskkar, and S. B. Rodríguez, "Open-circuit fault diagnosis and maintenance in multi-pulse parallel and series TRU topologies," *IEEE Trans. Power Electron.*, vol. 35, no. 10, pp. 10906–10916, Oct. 2020.
[18] C. Yang, D. Wu, Y. Liu, Q. Jia, and F. Zhang, "Diode open-circuit fault diagnosis based on hausdorff distance for autotransformer rectifier unit," in *Proc. 12th IEEE Energy Convers. Congr. Expo. - Asia*, 2021, pp. 1532–1536.
[19] Q. Du, L. Gao, W. Liu, X. Yin, and F. Meng, "Diode open-circuit fault research on the parallel-connected 24-pulse rectifier with DC-side passive harmonic reduction circuit," *IEEE Trans. Power Electron.*, vol. 37, no. 1, pp. 485–497, Jan. 2022.
[20] Q. Du, L. Gao, Q. Li, X. Yin, and G. F. Meng, "Diode open-circuit fault research on the parallel-connected 36-Pulse rectifier with dual passive harmonic reduction method," *IEEE Trans. Power Electron.*, vol. 37, no. 1, pp. 6821–6830, Jun. 2022.
[21] W. Li, W. Liu, W. Wu, X. Zhang, Z. Gao, and X. Wu, "Fault diagnosis of star-connected auto-transformer based 24-pulse rectifier," *Measurement*, vol. 91, pp. 360–370, Sep. 2016.
[22] Y. Lin, H. Ge, S. Chen, and M. Pecht, "Two-level fault diagnosis RBF networks for auto-transformer rectifier units using multi-source features," *J. Power Electron.*, vol. 20, pp. 754–763, Feb. 2020.
[23] F. Meng, L. Gao, S. Yang, and W. Yang, "Effect of single-phasing on multipulse rectifier with active interphase reactor," *IEEE Trans. Power Electron.*, vol. 30, no. 5, pp. 2549–2555, Mar. 2015.
[24] R. Kalpana, P. P. S., V. S. V., and B. Singh, "Investigations on open circuit faults of zigzag autoconfigured transformer based 12-pulse rectifier," *IEEE Trans. Ind. Appl.*, vol. 56, no. 2, pp. 1599–1608, Mar. 2020.
[25] B. An et al., "A new DC multi-pulse integrated shipboard power supply system and performance analysis referring to transformer non-integer turns ratio deviation," *IEEE Trans. Power Electron.*, vol. 36, no. 1, pp. 353–363, Jan. 2021.
[26] L. Yuan, Y. Wei, and Y. Shiyanf, "The influence of leakage inductance on multi pulse rectifier based on the modulation theory," in *Proc. IEEE 11th Conf. Ind. Electron. Appl.*, 2016, pp. 489–494.
[27] A. Sikora and B. Kulesz, "Influence of diode commutation processes on rectifier transformers operation," in *Proc. XIX Int. Conf. Elect. Mach.*, 2010, pp. 1–5.
[28] B. Wu, "Multipulse SCR rectifiers," in *High-Power Converters and AC Drives*. Hoboken, NJ, USA: Wiley, 2006, pp. 65–81.

Chao Yang was born in Jiangsu Province, China, in 1992. He received the M.S. degree in automation and electrical engineering from Jinan University, Jinan, China, in 2019. He is currently working toward the Ph.D. degree in electrical engineering with Nanjing University of Aeronautics and Astronautics, Nanjing, China.

His research interests include fault diagnosis and tolerance control of power converters.

Fanghua Zhang (Member, IEEE) received the B.S. degree in automation and electrical engineering from Jinan University, Jinan, China, in 1999, and the Ph.D. degree in electrical engineering from Nanjing University of Aeronautics and Astronautics (NUAA), Nanjing, China, in 2004.

He is a Professor with the Department of Electrical Engineering, NUAA. His research interests include high-frequency and high-density power conversion, high-frequency magnetic components, and dc microgrid.

Long Cheng received the M.S. degree in control engineering from Anhui University, Hefei, China, in 2015, and the Ph.D. degree in electrical engineering from Nanjing University of Aeronautics and Astronautics, Nanjing, China.

He is currently a Lecturer with the Department of Electrical Engineering, Anhui Agricultural University, Hefei, China. His research interests include power converters, energy storage technology, and dc power supply system.

Zhaorong Zhang was born in Hunan, China, in 1998. He received the B.S. degree from the Nanjing University of Aeronautics and Astronautics, Nanjing, China, in 2020, where he is currently working toward the M.S. degree in electrical engineering.

His research interests include multipulse rectifiers and high power factor rectifiers.